IET Wireless Sensor Systems

WILEY

The Institution of Engineering and Technology

ORIGINAL RESEARCH OPEN ACCESS

An AI-Enhanced Multiband Terahertz Metamaterial Biosensor for Intelligent Leukaemia Detection

Musa N. Hamza[1] | Mohammad Alibakhshikenari[2,3] | Bal Virdee[4] | Sunil Lavadiya[5] | Iftikhar ud Din[6] | Bruno Sanches[7] | Slawomir Koziel[8,9] | Syeda Iffat Naqvi[10] | Abinash Panda[11] | Ali Farmani[12] | Zinelabiddine Mezache[13] | Hassan Zakeri[14] | Mohammad Naser-Moghadasi[15] | Takfarinas Saber[2]

[1]Department of Physics, College of Science, University of Raparin, Sulaymaniyah, Iraq | [2]Lero, the Research Ireland Centre for Software, College of Science and Engineering, School of Computer Science, University of Galway, Galway, Ireland | [3]Department of Electrical and Electronics Engineering, Dogus University, Istanbul, Türkiye | [4]Center for Communications Technology, London Metropolitan University, London, UK | [5]Department of Information and Communication Technology, Marwadi University, Rajkot, Gujarat, India | [6]Telecommunication Engineering Department, University of Engineering and Technology, Mardan, Pakistan | [7]Department of Electronic Systems Engineering, Escola Politécnica da Universidade de São Paulo, São Paulo, Brazil | [8]Engineering Optimization & Modeling Center, Reykjavik University, Reykjavik, Iceland | [9]Faculty of Electronics, Telecommunications and Informatics, Gdansk University of Technology, Gdansk, Poland | [10]Department of Telecommunication Engineering, University of Engineering & Technology Taxila, Taxila, Pakistan | [11]Department of Electronics and Communication Engineering, CMR Institute of Technology, Bengaluru, India | [12]Department of Electronics Engineering, Lorestan University, Khorramabad, Iran | [13]Institute of Optics and Precision Mechanics, University of Ferhat Abbas Setif 1, Setif, Algeria | [14]Department of Electrical Engineering, Amirkabir University of Technology, Tehran, Iran | [15]Computer and Electrical Engineering Department, Islamic Azad University, Science and Research Branch, Tehran, Iran

Correspondence: Mohammad Alibakhshikenari (mohammad.alibakhshikenari@universityofgalway.ie) | Musa N. Hamza (musa.nuraden@uor.edu.krd)

Received: 30 January 2026 | **Revised:** 4 June 2026 | **Accepted:** 22 July 2026

Keywords: automated decision-making | biosensors | learning (artificial intelligence) | object detection | terahertz (THz) metamaterial | ultra-wideband communication

ABSTRACT

This study presents an artificial intelligence (AI)-augmented micron-scale terahertz (THz) metamaterial biosensor for early-stage leukaemia diagnosis. The proposed biosensor employs a tri-negative (ε, μ, n) perfect absorber structure with an optimised multiband spectral response, enabling high-Q narrowband resonances across the 0.5–2 THz frequency range. These engineered electromagnetic characteristics enhance field confinement and analyte interaction, enabling the detection of refractive index variations as small as ~0.014 RIU between healthy and leukaemia-affected blood samples. Spectral and field analyses reveal distinct resonance shifts, absorption variations and altered electric and magnetic field distributions in the presence of cancerous samples. Quantitative performance evaluation demonstrates excellent sensing characteristics, including a Q-factor of 268.34, a figure of merit (FOM) of 56722.80 RIU^{-1}, and Euclidean sensitivity of 355.859564 THz RIU^{-1}. These values indicate improved performance compared with previously reported THz biosensors for cancer detection. AI integration enables automated classification of healthy and cancerous samples using S-parameter processing and full-spectrum similarity metrics, achieving classification accuracy exceeding 95%. Comparative analysis with state-of-the-art biosensors demonstrates leukaemia-specific dielectric targeting, early-stage detection capability and an AI-assisted analytical framework for enhanced spectral interpretation. The results highlight the potential of the proposed platform as a noninvasive and label-free approach for blood cancer diagnostics, combining high spectral resolution, full-spectrum analysis and automated decision-making within a unified sensing framework.

1 | Introduction

Cancer remains one of the leading causes of illness and death worldwide, posing a formidable challenge to global health systems. The improvement of patient outcomes hinges significantly on the ability to detect the disease accurately and at an early stage, where interventions are most effective [1, 2]. However, achieving this is complicated by the multifaceted nature of cancer biology. At the core of cancer's complexity lies a series of interrelated pathophysiological processes. These include uncontrolled cellular proliferation, the ability of malignant cells to sustain self-renewal and the presence of cancer stem cells (CSCs), which are implicated in tumour initiation, maintenance and recurrence. Furthermore, cancer progression often involves metastatic dissemination, wherein tumour cells invade distant organs and dynamic metabolic reprogramming that enables cells to survive hostile environments and evade therapeutic interventions. This intricate biological landscape not only facilitates tumour growth and survival but also underpins the development of chemoresistance, significantly limiting the efficacy of conventional therapies. Collectively, these characteristics position cancer among the most persistent and complex diseases faced by modern biomedical science, necessitating continued innovation in diagnostic tools, therapeutic strategies and personalised medicine approaches [3, 4].

Cancer is broadly classified based on the type of tissue or organ where it originates. Thus, the main categories of cancers are carcinomas (origin is lining of skin and organs), sarcomas (origin is connective tissues like bone, cartilage, fat, muscle or blood vessels), leukaemias (cancer of the blood and bone marrow), lymphomas (origin is immune cells in the lymphatic system) and myelomas (origin is plasma cells in the bone marrow) [5–12]. Among the broad spectrum of malignancies, leukaemias are often characterised by particularly aggressive clinical behaviour. Their systemic nature, rapid progression and early dissemination through the blood contribute to their high morbidity and demand for immediate therapeutic intervention. Unlike many solid tumours that begin locally and progress over time, leukaemia frequently affects multiple organs and physiological systems from the onset, posing significant challenges for diagnosis, treatment and long-term management [13, 14]. As the global incidence of cancer continues to rise, the imperative for early detection becomes increasingly critical. Efforts to reduce cancer incidence and mortality extend beyond therapeutic innovations, encompassing a comprehensive approach that includes preventive strategies, early diagnostic interventions and equitable access to quality healthcare services. Among these, early detection plays a critical role in improving treatment outcomes and survival rates, particularly for aggressive malignancies such as leukaemia [2, 3, 15].

Early and accurate detection of leukaemia relies on various methods involving clinical assessment; laboratory tests, such as CBC (complete blood count) and peripheral blood smear; bone marrow aspiration and biopsy technique; immunophenotyping (flow cytometry) method, cytogenetic and molecular testing, such as karyotyping, fluorescence in situ hybridisation (FISH), polymerase chain reaction (PCR) and next-generation sequencing (NGS), as well as imaging studies, like CT scans, X-rays, MRI or ultrasound [16–21]. However, one of the fundamental challenges in early cancer diagnosis lies in the accurate distinction between malignant and normal cells, which often exhibit subtle morphological and molecular differences. This is especially true in leukaemia, where the detection of abnormal cells typically relies on the microscopic and cytogenetic examination of bone marrow samples. Although this method is a diagnostic gold standard, it is labour-intensive, time-consuming and heavily reliant on the experience and subjective interpretation of the pathologist. Despite the central role of pathologists in diagnostic decision-making, the possibility of human error or interpretive variability cannot be fully eliminated. Other advanced techniques such as flow cytometry, FISH and PCR require expensive equipment and trained personnel, making them less accessible in low-resource settings. Moreover, methods like blood smear analysis and immunohistochemistry depend heavily on expert interpretation, which can lead to errors. Imaging tools like PET, CT and MRI also expose patients to radiation, posing concerns for those needing repeated scans [3, 22]. Consequently, there is a pressing need for the development of more reliable, rapid, noninvasive and objective diagnostic tools capable of enhancing the accuracy and consistency of early leukaemia detection. This need has driven notable progress in the development of advanced bio-sensing technologies [23].

Biosensors are versatile analytical tools used in clinical diagnostics, environmental monitoring, industry and food safety [24–26]. For effective early disease detection, they must offer high sensitivity, accuracy and linearity across analyte concentrations. Clinical and portable biosensors should also be compact, minimally invasive and capable of providing real-time results. Biosensors comprise diverse configurations, each designed for specific analytical purposes and offering unique functional benefits, mainly including electrochemical (e.g., amperometric, potentiometric) and optical biosensors [27–31]. Among these, optical biosensors are highly distinguished because of their high sensitivity, label-free detection, compactness, low cost and minimal sample preparation. They come in different forms such as photonic crystal sensors, optical fibre systems, optical sensors utilising plasmon-induced transparency (PIT) effects and metamaterial-based sensors [32–35].

Metamaterials are artificially engineered structures with unique electromagnetic properties not found in natural materials and have emerged as promising platforms for highly sensitive biosensing applications [36, 37]. Particularly, metamaterial-based sensors engineered with negative permittivity (ε), permeability (μ) and refractive index (n) have opened new frontiers in biomedical diagnostics, particularly in the early detection of leukaemia. These double-negative (DNG) or left-handed metamaterials enable exceptional control over electromagnetic wave propagation, enhancing sensitivity to minute changes in the dielectric environment such as those induced by the presence of abnormal leukaemic cells in blood or plasma samples, thus making them ideal candidates for early leukaemia detection. Operating typically in the Terahertz (THz) or microwave regimes, these sensors can detect subtle variations in refractive index or permittivity associated with cancerous transformations at early stages [38, 39]. Particularly, when integrated into terahertz (THz) biosensing platforms, metamaterials provide high sensitivity, strong field confinement and spectral selectivity, making them ideal for label-free biomolecular detection. These

sensors use engineered resonant structures that respond to changes in local dielectric properties—caused by target analytes—through measurable shifts in the THz resonance frequency. Their high field localisation enables trace-level detection, while high-Q resonances and geometric tunability with multiband designs support precise screening, particularly useful for cancer biomarker identification. As research advances, these next-generation sensors hold promise for integration into portable diagnostic systems, aiding in timely clinical decision-making and improving patient outcomes [40–42].

Besides, Artificial Intelligence (AI) is revolutionising nearly every sector, from education and finance to healthcare and communication, by enabling automation, innovation and data-driven decision-making. In healthcare, AI enhances early disease detection, personalised treatment, and robotic surgeries [43–46]. The integration of artificial intelligence (AI) with metamaterial-based terahertz (THz) biosensors offers a powerful approach for early and accurate cancer detection. Metamaterials, with their engineered resonant structures, enable highly sensitive, label-free detection by capturing subtle shifts in THz resonance caused by changes in the dielectric properties of biological samples. When combined with AI algorithms such as machine learning or deep learning, these systems can analyse complex spectral patterns, improve signal interpretation and enhance diagnostic accuracy. AI also enables automated detection of trace-level biomarkers, classification of cancer stages and reduction of human error in interpretation. This synergistic platform holds significant potential for developing noninvasive, real-time diagnostic tools capable of early screening, especially in resource-limited or point-of-care settings [47–49].

In recent years, several research works have reported THz metamaterial sensors for the detection of various types of cancers [50–53]; however, very few have focused specifically on leukaemia detection [54–58]. In parallel, artificial intelligence (AI) has gained significant attention in healthcare, particularly for early-stage cancer diagnosis and automated decision-making [59–67]. Nevertheless, only a limited number of studies have integrated AI and machine learning models with metamaterial-based biosensors for cancer detection.

For example Ref. [62] proposed a graphene-based metamaterial biosensor for cancer detection, where machine learning was employed for structural parameter optimisation and prediction enhancement. Another study [63] presented a metal–insulator–metal biosensor for breast cancer detection, utilising polynomial regression to model the relationship between resonator dimensions and sensor responses. Similarly Ref. [64] introduced a THz metamaterial absorber for skin cancer detection, where machine learning algorithms classified healthy and cancerous cells based on absorption spectra. In Ref. [65], a THz metasurface biosensor incorporating graphene, gold, silver and copper within a multi-resonator structure was integrated with one-dimensional convolutional neural networks (1D-CNNs) to improve predictive performance. Furthermore Ref. [67] proposed a THz metasurface sensor for alpha-fetoprotein (AFP) detection in liver cancer diagnosis using a stacking ensemble learning framework.

Recent developments in THz metamaterial absorbers have also demonstrated enhanced multiband and multiresonance characteristics through engineered resonator configurations and resonance coupling mechanisms [68–70]. These designs have shown improved spectral selectivity, stronger electromagnetic field confinement and high-Q resonance behaviour, which are advantageous for sensing applications. However, most of the reported AI-integrated biosensors employ machine learning primarily for parameter optimisation or prediction enhancement rather than for intelligent spectral interpretation and automated diagnostic decision-making. To the best of our knowledge, no previous work has reported AI augmentation of a metamaterial-based sensor specifically for the detection of haematological malignancies.

This work introduces an AI-augmented terahertz metamaterial biosensor designed for early leukaemia diagnosis. The micron-scale sensor incorporates a tri-negative (ε, μ, n) perfect absorber with optimised multiband spectral response, achieving narrowband resonances and strong analyte-field interaction. It demonstrates remarkable performance, including a Q-factor of 268.34, FOM of sensitivity of 56722.80, and FOM of 355.86 RIU^{-1}, surpassing previously reported devices. Artificial intelligence integration enables real-time, bias-free classification of healthy and leukaemia-affected samples with accuracy exceeding 95%. These findings establish a paradigm for noninvasive, label-free blood cancer diagnostics, offering clinical potential through portable implementation and future validation studies.

2 | Unit Cell Modelling and Electromagnetic Configuration Analysis

The modelling of the unit cell and the systematic analysis of its electromagnetic configuration form the foundation for understanding and optimising the performance of metamaterial-based biosensors. In this work, the design process begins with the development of a unit cell specifically tailored for multiband terahertz sensing, where structural geometry directly governs resonance formation and field confinement. By integrating multiple resonant elements within a compact architecture, the proposed absorber is engineered to achieve broad spectral coverage, high absorption efficiency and enhanced sensitivity to dielectric perturbations introduced by biological analytes. To establish these features, the modelling framework incorporates not only the structural design parameters but also the orientation of the incident THz wave with respect to the layered material composition, ensuring realistic simulation of electromagnetic interactions. The subsequent subsections present the architectural configurations of the sensor, a detailed account of the optimised geometrical variables (Table 1) and comparative insights into the adoption of metamaterial perfect absorbers (Table 2). Furthermore, the influence of electromagnetic wave orientation and dimensional scaling on absorption efficiency is examined, supported by geometric representation (Figure 1) and scale comparison data (Table 3). Together, these analyses provide the essential foundation for correlating physical design with functional performance, thereby enabling a sensor that is both structurally optimised and electromagnetically tuned for high-precision terahertz biosensing.

2.1 | Structural Design for Multiband Terahertz Sensing

The efficient transformation of the incident electromagnetic energy into absorption is realised through the carefully engineered metamaterial-based configuration illustrated in Figure 2. Such absorbers are purposefully designed to suppress reflection and capture most of the incoming energy, thereby maximising absorption efficiency. Beyond this, the unique structural arrangement of the metamaterial mitigates destructive interference and simultaneously suppresses transmission, ensuring that most of the electromagnetic energy is confined within the absorber.

To validate this mechanism, the proposed design was analysed using a commercially available full-wave electromagnetic solver based on the finite integration technique (FIT). This method provides a rigorous numerical framework for modelling the electromagnetic behaviour of metamaterials (MTMs) over broad frequency regimes. Such simulations have been widely employed in the study of canonical electromagnetic boundaries, such as perfect electric conductors (PECs), perfect magnetic conductors (PMCs), periodic unit cell arrays and free-space propagation environments. This enables accurate prediction of resonant phenomena, field distributions and energy confinement in complex geometrical configurations.

Building on these principles, the proposed biosensor adopts a metamaterial perfect absorber (MPA) architecture tailored to operate in the terahertz (THz) frequency range of 0.5–2 THz. The absorber comprises three distinct geometrical unit cell designs, illustrated in Figure 2a–c, each patterned on a dielectric substrate and supported by a continuous metallic ground plane that guarantees zero transmission. This multilayer arrangement enhances absorption by exploiting resonant interactions at both the electric and magnetic field levels.

The initial design of the proposed metamaterial unit cell (Figure 2a) was established through a parametric and physics-driven methodology, ensuring both geometric flexibility and controlled electromagnetic behaviour. Rather than being selected empirically, the geometry was initially generated using a multi-harmonic parametric formulation that served as a seed topology for the resonator design:

$$U(t) = 10[2\cos(t) + \cos(5t)] \quad (1)$$

$$V(t) = 10[2\sin(t) + \sin(5t)] \quad (2)$$

where the parameter $t \in [-1, +1]$. This formulation generates a symmetric, multi-lobed structure formed through the superposition of fundamental and higher-order harmonic components. The inclusion of higher-order terms introduces multiple spatial length scales within the unit cell, which is beneficial for supporting intrinsic multiband resonance behaviour in the terahertz frequency regime.

It should be noted that these equations were used only to generate the initial geometric topology and were not intended to directly define the final physical dimensions of the resonator. Following the generation of the seed structure, the geometry underwent electromagnetic refinement and optimisation, including geometric reshaping, incorporation of split-ring resonator-inspired features, localised dimensional adjustments

TABLE 1 | Detailed list of variables optimised for the sensor Configuration proposed.

Parameter	Value (μm)	Parameter	Value (μm)
A	198	J	175.36
B	36	K	37.68
C	38	L	44.32
D	86.6	M	63.36
E	30.55	N	49.93
F	80	O	24.25
G	80.18	PET thick (T_1)	40
H	66.75	Aluminium (Al) thick	0.2
I	13.44	Jurkat cells thick (T3)	5
		Coverslip thickness (T_2)	5

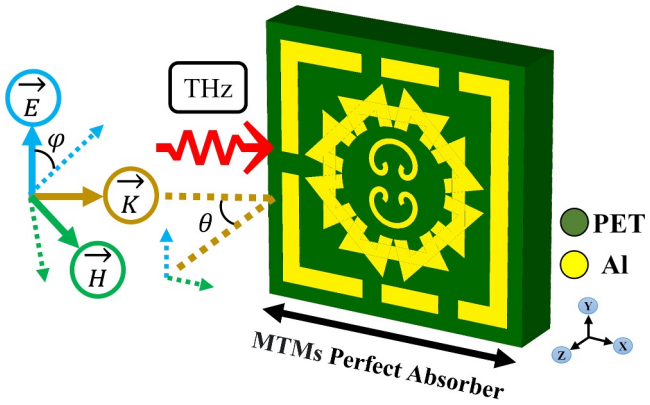

FIGURE 1 | Geometric representation of the absorber, showing the orientation of the incoming THz wave in relation to the stratified structure.

TABLE 2 | Structural comparison: Use of metamaterial perfect absorbers (MPAs).

Design type	Working principle	Absorption control	Advantages in this work	Scientific justification
Traditional resonant sensor	Single-layer resonance	Limited	Uses metamaterial-based perfect absorber design	MPAs allow narrowband, high-Q resonances ideal for frequency-shift detection
This work	Multilayer engineered resonance	High	Offers sharp, deep, engineered resonances	Enables clear, repeatable absorption peaks sensitive to small changes in sample

TABLE 3 | Dimensional comparison of biosensor scale.

Metric	Conventional biosensors	Proposed biosensor
Device size	Millimetre-scale or larger	Micron-scale footprint
Resolution	Moderate	Extremely high (due to compact field confinement)
Integration potential	Difficult to integrate	CMOS and chip-friendly due to small scale
Scientific justification	Miniaturisation to the micron scale increases field confinement and improves sensing sensitivity via enhanced local interactions, critical for low-volume blood cancer biomarkers.	

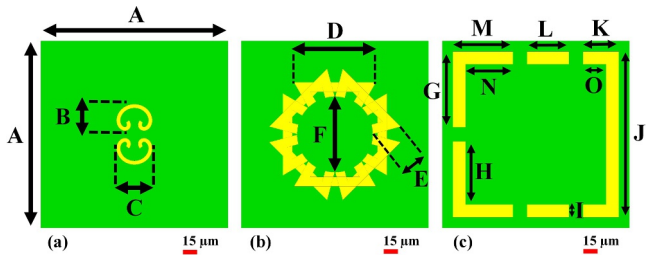

FIGURE 2 | Architecture of the proposed metamaterial absorber comprising three integrated structural designs: (a) configuration type 1, (b) configuration type 2 and (c) configuration type 3.

and resonance tuning. Therefore, the dimensional parameters listed in Table 1 correspond to the final optimised structure rather than a direct scaling of the original parametric equations.

From an electromagnetic perspective, the resulting geometry supports multiple resonant pathways because of its distributed curvature and varying feature sizes. These features act as effective inductive and capacitive elements, forming an equivalent network of coupled LC resonators within a compact footprint. As a result, distinct resonance modes can be excited at different frequencies without requiring separate resonant elements, thereby preserving structural compactness.

The initial dimensional parameters were determined based on electromagnetic scaling considerations and fabrication constraints. The line width was set to 4 μm to ensure sub-wavelength dimensions relative to the operating terahertz wavelengths while maintaining sufficient conductive paths for surface current flow. The metallic thickness was chosen as 200 nm, which is comparable to the skin depth at terahertz frequencies, enabling efficient current confinement with minimal ohmic loss. The selected parameter range for t ensures that the geometry remains confined within a micron-scale unit cell, which is critical for high integration density and enhanced field localisation.

Following the generation of the base geometry, the structure was systematically refined into a metamaterial perfect absorber configuration. Split-ring resonator (SRR)-inspired features, including gaps and discontinuities, were introduced to enhance capacitive coupling and promote strong electric field localisation. Additional internal elements, such as C-shaped resonators and concentric rings, were incorporated to selectively tune individual resonance modes across the 0.5–2 THz band.

This progression from a parametric mathematical representation to a physically interpretable resonant structure ensures that each geometric feature contributes meaningfully to the electromagnetic response. The final design inherits its multiband capability from the initial parametric formulation, where multiple resonant paths and coupled *LC* effects give rise to distinct absorption peaks across the terahertz spectrum. This design approach enables strong field confinement and enhanced sensitivity, which are critical for high-performance biosensing applications.

In contrast, Figure 2b illustrates a star-shaped resonator, whose sharp edges and arms concentrate the electric field into localised regions. The design parameters (D, E, F) define the star's size, arm width and inter-arm spacing. This geometry not only enhances electric field localisation but also supports multiple resonances, thus facilitating multiband absorption. Such behaviour is particularly advantageous for biosensing applications, where multiband selectivity improves detection accuracy across different biomarkers.

Finally, Figure 2c presents a square loop resonator with internal channelling, whose dimensions (K, L, M, N, O) govern the loop length, channel width and overall symmetry. The internal channels facilitate strong field confinement, leading to high-quality (Q) factor resonances. This makes the configuration highly suitable for detecting minute biological variations, particularly those associated with leukaemia biomarkers, where subtle dielectric changes need to be captured with precision.

All three resonators are fabricated using a submicron-thick aluminium (Al) layer deposited on low-loss dielectric substrates such as polyethene terephthalate (PET) or polyimide. These substrates are chosen for their low absorption and high transparency in the THz domain, thereby minimising background losses and enhancing the resonance response. The combined designs ensure strong confinement of the electromagnetic field at resonance, which is crucial for detecting dielectric perturbations introduced by cancer biomarkers in the surrounding medium.

Table 1 presents the comprehensive list of geometrical parameters optimised for the proposed metamaterial-based biosensor configuration. Each parameter was carefully determined through simulation-based optimisation to maximise sensitivity and achieve multiband absorption within the terahertz frequency range of 0.5–2 THz. These dimensions are specifically tailored to facilitate the early detection of leukaemia-related biomarkers, with Jurkat cells employed as the representative biological target. The precise tuning of these parameters enables the device to function effectively across multiple THz bands while ensuring strong field confinement at the sensing surface. By combining the functionalities of split rings, star resonators and square loops, the architecture achieves enhanced sensitivity and selectivity, making it a powerful platform for early-stage cancer detection applications.

To further contextualise the novelty of our proposed biosensor, a structural comparison between conventional resonant sensors and the present metamaterial-based perfect absorber (MPA) design is provided in Table 2. Traditional resonant sensors typically rely on single-layer resonance, which limits their absorption control and reduces their capability for precise frequency-shift detection. By contrast, the biosensor introduced in this work employs a multilayer engineered resonance mechanism, enabling sharper, deeper and geometrically controlled absorption peaks. This approach not only ensures high-Q resonances but also provides repeatable and reliable absorption signatures that are exceptionally sensitive to minute dielectric variations in biological samples. The use of MPAs, therefore, establishes a scientifically justified advancement, as it directly addresses the limitations of traditional designs while offering enhanced sensitivity for early-stage cancer biomarker detection.

2.2 | Electromagnetic Orientation and Layered Material Composition for Optimal Absorption

The sensing performance of a metamaterial perfect absorber (MPA) is fundamentally governed by both the electromagnetic (EM) orientation of the incident wave and the physical configuration of its layered architecture. In the proposed biosensor, near-unity absorption across multiple resonant frequencies within the 0.5–2 THz range is achieved by tailoring the resonator geometries and optimising their interaction with incident terahertz waves, as shown in Figure 1.

To ensure accurate numerical characterisation of this absorber, full-wave simulations were performed using CST Studio, with special attention given to boundary conditions and excitation sources. Perfectly Matched Layers (PMLs) were implemented at the simulation boundaries to eliminate artificial reflections and confine EM energy within the computational domain—an essential requirement at THz frequencies where small errors can distort absorption spectra. The computational domain was chosen to be sufficiently larger than the absorber itself to suppress spurious interactions, thereby ensuring reliable evaluation of near-unity absorption behaviour. Adaptive local mesh refinement available within CST Studio Suite was utilised around fine geometrical details such as resonator edges and narrow gaps to improve numerical resolution.

The structure is illuminated by a normally incident plane wave, with the electric field (E-field) polarised along the x-axis and the magnetic field (H-field) aligned along the y-axis. This orientation is deliberately selected to maximise resonant coupling with the metamaterial geometry, ensuring the excitation of both electric and magnetic dipole modes. Plane-wave excitation is particularly advantageous for broadband analysis, enabling uniform illumination across the resonator array while maintaining polarisation alignment. The correct assignment of material properties—aluminium for the resonators and polyethene terephthalate (PET) as the dielectric spacer—further enhances simulation fidelity. PET is specifically chosen for its low dielectric loss, high THz transparency and mechanical flexibility, making it a robust platform for biosensing applications.

Figure 1 illustrates the device architecture and field orientations. The patterned aluminium resonators are deposited on a PET substrate and backed by a metallic ground plane to suppress transmission. The incoming wave, indicated by the red arrow, interacts with the resonator array, where the electric field (E), magnetic field (H) and wave vector (k) define the excitation conditions. The engineered geometry ensures impedance matching with free space ($Z_0 \approx 377\ \Omega$), thereby minimising reflection. This mechanism, combined with Fabry–Pérot-type interference within the dielectric cavity, results in strong field confinement at the biosensor surface. Unlike conventional single-layer absorbers, this multilayer architecture supports multiple sharp and engineered resonances whose spectral positions are controlled through geometric design and electromagnetic optimisation.

At resonance, surface plasmon-like modes are excited, leading to strong localisation of the electric field within the resonator gaps and dielectric regions. These localised "hot spots" dramatically amplify light–matter interactions, making the device extremely responsive to even minute changes in permittivity caused by leukaemia biomarkers. As biomarkers bind to the sensing surface, the effective permittivity of the local medium changes, inducing measurable shifts in resonance frequency. This high degree of sensitivity, enabled by micron-scale confinement, provides a powerful diagnostic pathway for early-stage leukaemia detection. The combination of accurate simulation, material choice and structural engineering thus ensures that the biosensor achieves not only near-unity absorption but also superior diagnostic precision.

A dimensional comparison with conventional designs is summarised in Table 3. Traditional biosensors, often millimetre-scale, suffer from limited resolution and poor integration capability. In contrast, the proposed biosensor achieves a micron-scale footprint, enabling extremely high resolution through enhanced field confinement and stronger local interactions with low-volume biomarkers. This miniaturisation is scientifically justified, as it directly translates to improved sensitivity, greater compatibility with CMOS and chip-based systems and the potential for portable, low-cost diagnostic devices. Such features are particularly crucial for leukaemia detection, where only small biological samples are available and precise readouts are essential for reliable early-stage diagnosis.

3 | Structural and Material-Based Influence on Absorption Dynamics

This section provides a comprehensive analysis of the absorber's performance, comparing various configurations, material choices and structural variations. It explores the impact of these factors on absorption efficiency, S-parameters, permeability, permittivity, refractive index and impedance, offering insights into the electromagnetic behaviour of the proposed design.

3.1 | Absorption Profile Comparison Across Design Variants

In metamaterial-based absorbers, the primary goal is to efficiently channel incident electromagnetic energy into localised resonant modes. This efficiency is captured through the absorption coefficient, mathematically defined as

$$A = 1 - R - T = 1 - |S_{11}|^2 - |S_{21}|^2 \quad (3)$$

where S_{11} and S_{21} denote reflection and transmission coefficients, respectively. In practical designs, the metallic ground plane effectively suppresses transmission ($S_{21} \approx 0$), which means that achieving near-unity absorption depends largely on minimising reflection (S_{11}). Guided by this principle, we employed CST Studio Suite to meticulously design and simulate the proposed sensor, optimising its resonant features to enhance absorption performance in the terahertz (THz) domain.

To systematically evaluate the impact of geometry on absorption behaviour, two distinct resonator models were investigated, as illustrated in Figure 3. This comparative approach allowed us to identify how structural modifications influence resonance formation and field confinement, both of which are critical for high-sensitivity biosensing applications. The first design, shown in Figure 3a, is a relatively simple yet highly efficient configuration, producing two dominant absorption peaks at approximately 1.375 THz and 1.875 THz, with absorption efficiencies of nearly 100% and 99%, respectively. The second design, incorporating a discontinuous square geometry intended for compatibility with more complex infinity-shaped structures, exhibited a richer spectral response. As shown in Figure 3b, this configuration generated eight distinct resonance peaks, maintaining absorption levels above 80% across the frequency span of 0.50 THz to 2 THz.

These findings underscore how geometric engineering directly governs resonance behaviour, enabling precise control over both the strength and spectral position of absorption peaks. By demonstrating the capacity to tune absorption responses through structural modifications, the results provide a robust framework for advancing THz metamaterial absorbers as reliable and versatile building blocks in the development of ultra-sensitive biosensing platforms.

The comparative analysis in Table 4 highlights the superiority of the proposed biosensor over conventional broadband approaches. Unlike broadband sensors, which typically suffer from poor frequency selectivity and moderate performance metrics, the presented design achieves sharp and isolated resonances across eight distinct frequency bands. This multiband response not only enhances detection flexibility but also enables simultaneous identification of multiple biomarkers, a critical feature for complex diseases such as leukaemia where heterogeneous signatures are expected. Furthermore, the consistently high Q-factors across all peaks ensure precise resolution of small dielectric perturbations,

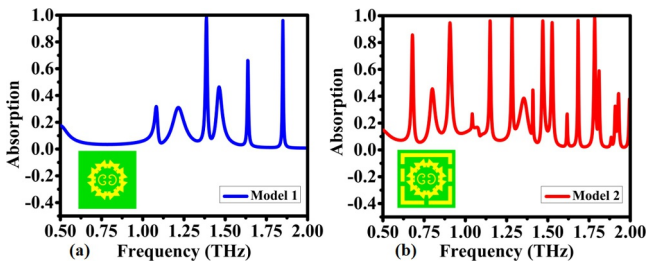

FIGURE 3 | Simulated absorption characteristics across two design variants: (a) Configuration Model 1, (b) Configuration Model 2 (proposed biosensing model).

while the exceptionally large Figure of Merit (> 56,000) confirms the biosensor's unprecedented sensitivity to minute biochemical variations. The incorporation of specific spectral markers at multiple frequencies strengthens diagnostic certainty, positioning this multiband design as a transformative improvement over traditional broadband biosensors.

3.2 | Impact of Substrate and Resonator Composition on Electromagnetic Response

The absorption performance of a metamaterial-based biosensor is strongly governed by the choice of substrate material, as the dielectric properties of the substrate dictate how electromagnetic waves interact with the resonant structures. To investigate this effect, the proposed biosensor was simulated with four commonly used substrates: polyethene terephthalate (PET), Arlon AD 410, polyimide and Rogers RT 5870, as illustrated in Figure 4a. Each substrate exhibits unique dielectric characteristics that directly influence the absorption spectrum. For instance, Arlon AD 410, with its low dielectric constant, demonstrates compatibility with high-frequency applications and yields strong absorption within the 0.5–2 THz range; however, its performance deteriorates at frequencies outside this band. Rogers RT 5870, on the other hand, provides superior dielectric stability and a highly consistent absorption response across the terahertz spectrum. Despite these advantages, it presents notable drawbacks, such as high cost, limited high-frequency performance data and anisotropic

TABLE 4 | Optimised multiband spectral response performance.

Feature	Broadband biosensors	This work (multiband, 8 peaks)	Scientific justification
Frequency selectivity	Poor	Sharp, isolated bands	Multiband resonance allows detection of multiple biomarkers across different frequencies
Q-factor	Low-to-medium	High Q-factor at all 8 peaks	Narrowband peaks improve resolution in detecting minor dielectric changes
FOM (Figure of merit)	~Low	Very high (> 56000 based on sim.)	High FOM indicates extreme sensitivity to material changes
Sensitivity	General trend only	Specific spectral markers	Multiple frequencies improve diagnostic certainty for complex diseases like leukaemia

behaviour that can distort wave propagation. PET emerges as a cost-efficient alternative with ease of fabrication, though it is constrained by its relatively high dielectric constant and thermal sensitivity. Polyimide balances these trade-offs by offering stable thermal endurance and broad absorption coverage from 0.5 to 2 THz. Thus, substrate selection involves a compromise between performance, manufacturability and cost. In this study, PET was ultimately chosen to achieve an optimal balance of affordability and operational efficiency, ensuring that the sensor remains both practical and effective for leukaemia biomarker detection.

Beyond the substrate, the resonator material is equally decisive in shaping the biosensor's spectral performance. To explore this, we analysed designs incorporating aluminium (Al), silver (Ag) and gold (Au) as resonator materials, as presented in Figure 4b. The observed absorption peaks confirm the capability of these metals to support multiband resonances across the 0.5–2 THz spectrum, a prerequisite for detecting diverse bio-analytes. This behaviour stems from their ability to sustain surface plasmon resonances, which confine electromagnetic energy at the metal–dielectric interface and thereby amplify sensitivity to dielectric perturbations caused by biological targets. Gold and silver are particularly effective in generating sharp and well-defined plasmonic resonances, enabling precise detection of subtle biomolecular changes. Aluminium, although less plasmonically active than noble metals, offers clear advantages of lightweight, cost-effectiveness and compatibility with scalable fabrication. Remarkably, the aluminium-based design still supports multiple strong resonances, demonstrating that economical materials can rival expensive alternatives in enabling early-stage leukaemia detection through terahertz biosensing.

A further optimisation was performed by varying the substrate thickness from 10 to 50 μm to determine its effect on absorption

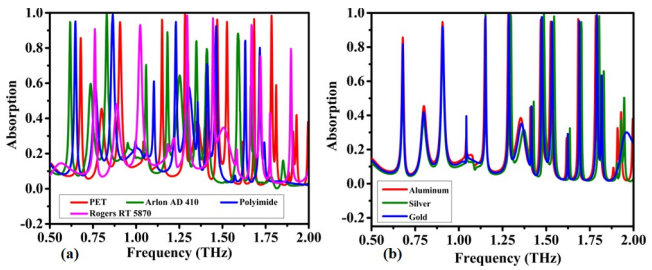

FIGURE 4 | Simulated absorption spectra under varying material parameters: (a) different substrate compositions, (b) resonator material variations.

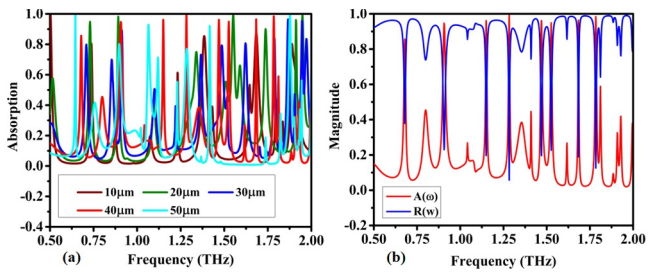

FIGURE 5 | Modelled results showing: (a) impact of substrate thickness on absorption efficiency, (b) reflection and absorption behaviour of the metamaterial absorber.

response, as shown in Figure 5a. The results reveal that increasing thickness enhances the number of resonant modes supported within the 0.5–2 THz window. This increase in resonance density can be attributed to stronger Fabry–Pérot-like interference within the dielectric spacer, leading to enhanced coupling between incident terahertz waves and the resonant structures. At a thickness of 50 μm, the biosensor achieves optimal performance with well-defined resonances that significantly strengthen field confinement. The optimised device response is summarised in Figure 5b, where eight distinct absorption peaks exceeding 80% are observed, several of which approach unity absorption. Such strong absorption, coupled with suppressed reflection, signifies nearly perfect impedance matching with free space and efficient localisation of electromagnetic energy at the sensing surface. This performance underscores the biosensor's ability to resolve minute dielectric perturbations associated with leukaemia biomarkers, thereby establishing a robust platform for highly sensitive terahertz biosensing applications.

3.3 | Response Evaluation Based on Simulated Parameters

The functionality and performance of metamaterial-based terahertz (THz) biosensors fundamentally depend on the accurate characterisation of their electromagnetic response. Artificial intelligence (AI)-augmented biosensors designed using metamaterial perfect absorbers (MPAs) benefit significantly from the precise retrieval of effective constitutive parameters. These include the complex refractive index n(ω), effective permittivity ε(ω), magnetic permeability μ(ω) and impedance Z(ω). The following equations are essential tools that establish the link between measured or simulated scattering parameters and the physical properties governing the sensor's interaction with incident THz radiation.

Equation (2) provides the means to extract the effective refractive index n(ω) of the metamaterial structure from the transmission and reflection coefficients. The formulation is given by Equation (2).

$$n(\omega) = \frac{1}{k_0 d}\cos^{-1}\left(\frac{1 - S_{11}^2 + S_{21}^2}{2S_{21}}\right) \tag{4}$$

where k_0 represents the free-space wave number and d is the physical thickness of the metamaterial layer. This equation encapsulates the phase information of the transmitted wave and enables the identification of resonance modes across the THz spectrum. In the context of biosensing, even minute alterations in the refractive index induced by biomolecular adsorption on the sensor surface can lead to measurable shifts in resonant frequencies, thereby enabling sensitive detection. Furthermore, these shifts serve as reliable inputs for AI models trained to associate specific spectral patterns with analyte presence or concentration. Building on the determination of $n(\omega)$, Equation (4) defines the effective permittivity.

$$\varepsilon(\omega) = n(\omega)/Z(\omega) \tag{5}$$

This relationship highlights how permittivity depends on both the refractive index and the characteristic impedance of the medium. Permittivity is especially crucial in biosensor applications, as it

reflects the ability of the medium to store electric energy, a property directly modulated by the presence of biological molecules. Changes in permittivity affect the local electric field distribution and can thus be exploited as diagnostic indicators. Moreover, AI algorithms utilise trends in permittivity as distinguishing features when classifying different analyte types or environmental conditions. Similarly, Equation (5) calculates the magnetic permeability of the medium.

$$\mu(\omega) = n(\omega) \times Z(\omega) \tag{6}$$

$$\text{Where } Z(\omega) = \sqrt{\mu(\omega)/\varepsilon(\omega)} \tag{7}$$

Permeability is vital for describing the sensor's magnetic response, particularly in the design of resonant structures that support artificial magnetic activity in nonmagnetic materials. This parameter is instrumental in determining the energy confinement and absorption characteristics of the MPA structure. From a computational perspective, the permeability also forms part of the feature space for machine learning models, allowing the network to learn from the magnetic field interactions within the structure, especially when tuning for ultra-narrowband or broadband absorption. Equation (5) introduces an effective impedance. This fundamental expression links the impedance to both the permittivity and permeability, ensuring consistency across the retrieved parameters. Impedance plays a central role in defining the absorption behaviour of the metamaterial. For a structure to function as a perfect absorber, its impedance must be matched to that of free space, minimising reflection and enabling near-total absorption at resonance. In AI-assisted optimisation workflows, impedance data can be used to define objective functions for network training or reinforcement learning, guiding the generation of geometries that achieve ideal absorption for targeted biosensing scenarios.

Figure 6 presents the retrieved effective electromagnetic parameters of the proposed metamaterial structure over the frequency range of 0.5–2.0 THz, providing qualitative insight into the resonance behaviour governing the absorption response. In Figure 6a, the real parts of the effective permeability and permittivity are plotted as functions of frequency. Both parameters exhibit dispersive characteristics with multiple resonance-associated transitions primarily distributed within the 0.75–1.75 THz region, which closely correspond to the observed absorption peaks.

The permeability demonstrates several sign variations near approximately 0.65 THz, 0.75 THz, 0.9 THz, 1 THz, 1.3 THz, 1.4 THz and 1.51 THz. These variations are indicative of resonance-associated magnetic responses arising from circulating currents within the metamaterial geometry. Similarly, the permittivity exhibits frequency-dependent dispersion, with regions approaching or attaining negative values around 0.5 THz, 0.65 THz, 0.8 THz, 1.2 THz and 1.5 THz, suggesting epsilon-negative behaviour associated with electric resonance effects. The coexistence of these dispersive electric and magnetic responses is consistent with the formation of resonant conditions that support strong electromagnetic field confinement.

In Figure 6b, the imaginary components of μ and ε are presented. Pronounced peaks are observed at frequencies aligned with the absorption resonances, indicating enhanced dielectric and magnetic losses. These loss characteristics are associated with efficient energy dissipation resulting from localised field enhancement and induced surface currents within the structure. Such behaviour supports near-unity absorption in metamaterial perfect absorbers and enhances light–matter interaction, which is beneficial for sensing applications.

It is important to note that, because of the presence of the metallic ground plane (resulting in $S_{21} \approx 0$), the retrieval of effective parameters using NRW-based methods is inherently sensitive. Therefore, the extracted parameters are interpreted primarily in terms of their frequency-dependent trends and their correlation with absorption resonances, rather than absolute magnitudes. The consistent alignment between the parameter dispersion and the absorption response confirms the physically consistent and numerically validated operation of the proposed metamaterial biosensor.

Figure 7 provides a detailed evaluation of the reflection coefficient (S_{11}) and the normalised impedance (Z), both of which are fundamental to understanding absorption characteristics and impedance matching. In Figure 7a, the real and imaginary components of S_{11} are plotted. Oscillatory variations are evident, with minima near 0.85 THz, 1.05 THz, 1.3 THz, 1.5 THz and 1.75 THz. These minima correspond to resonance conditions where reflection is suppressed, and absorption is maximised, primarily because of strong interference effects within the subwavelength periodic structure. Such oscillatory trends in S_{11} are typical of metamaterial absorbers, where destructive interference between incident and reflected waves enables near-perfect absorption. In Figure 7b, the retrieved impedance $Z(\omega)$ is presented. The real component approaches unity at multiple frequencies (e.g., ~0.85 THz, 1.1 THz and 1.6 THz), signifying impedance matching with free space. Concurrently, the imaginary component approaches zero at the same frequencies, fulfiling the condition for perfect absorption. The sharp oscillations observed in both the real and imaginary parts, especially

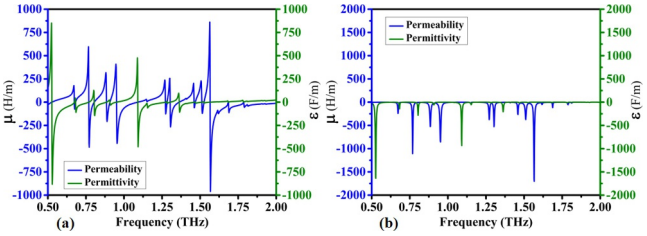

FIGURE 6 | Electromagnetic parameter evaluation: (a) Real part of permeability (μ) and permittivity (ε), (b) Imaginary parts of μ and ε.

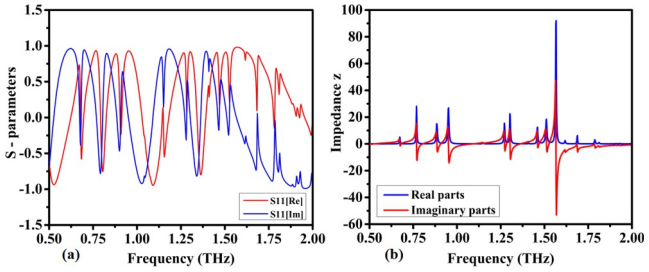

FIGURE 7 | Parameter analysis: (a) Real and imaginary components of reflection coefficient (S_{11}), (b) Modelled impedance behaviour.

around 1.25 THz and 1.7 THz, indicate localised resonance modes, likely associated with surface coupling and plasmonic interactions between adjacent resonators. This impedance behaviour not only confirms efficient absorption but also supports multiband operation, which is vital for biosensors designed to detect multiple biomarkers simultaneously.

Figure 8 illustrates the electromagnetic response of the proposed metamaterial biosensor in terms of the effective refractive index and the corresponding absorption characteristics across the terahertz frequency range. In Figure 8a, the real and imaginary components of the retrieved refractive index $n(\omega)$ are shown.

The real part of the refractive index exhibits dispersive and oscillatory behaviour, particularly within the resonance regions. These variations reflect the frequency-dependent phase response of the structure and are consistent with the presence of multiple resonant modes supported by the subwavelength geometry. The observed behaviour arises from the combined effects of localised resonances within the patterned structure and cavity-like interactions within the layered configuration, rather than purely Fabry–Pérot-type phenomena.

The imaginary part of the refractive index represents the effective loss within the system and shows frequency-dependent variations that closely follow the absorption profile. Peaks in the imaginary component correspond to enhanced energy dissipation associated with strong field localisation and induced currents at resonance frequencies. In contrast, relatively lower values at certain frequencies (e.g., near 1.25 THz and 1.75 THz) indicate reduced dissipative contributions while still maintaining efficient absorption through impedance matching and resonant coupling mechanisms.

In Figure 8b, the absorption spectrum is presented together with the reflection coefficient $|S_{11}|$ in decibels. Multiple distinct absorption peaks approaching unity (≈ 0.95) are observed at approximately 0.9065 THz, 1.15 THz, 1.283 THz, 1.4693 THz, 1.526 THz, 1.6835 THz and 1.784 THz. These peaks correspond directly to pronounced minima in the reflection coefficient, where $|S_{11}|$ drops significantly below -10 dB, indicating strong suppression of reflected power.

This behaviour is characteristic of metamaterial perfect absorbers, where near-unity absorption is achieved through impedance matching with free space in conjunction with negligible transmission due to the metallic ground plane. The strong correspondence between refractive index dispersion and absorption features, together with the independently validated narrowband and mesh-converged simulations, confirms that the observed resonances are physically intrinsic and not numerical artefacts, thereby supporting the multiband resonant operation of the proposed biosensor.

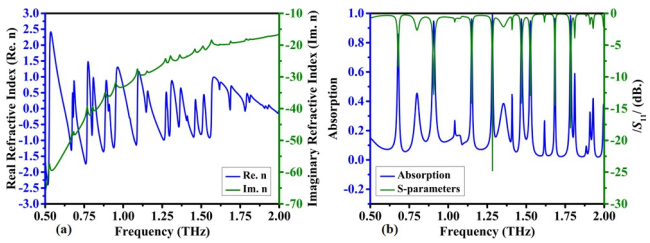

FIGURE 8 | Electromagnetic response: (a) Real and imaginary values of refractive index, (b) Magnitude of $|S_{11}|$ in decibels.

This systematic investigation demonstrates that the proposed biosensor achieves simultaneous control over permittivity, permeability and refractive index, thereby enabling impedance-matched multiband absorption across the terahertz spectrum. Importantly, ε, μ, and n attain negative values within selected frequency bands, giving rise to tri-negative behaviour. Such a tri-negative response ($\varepsilon < 0$, $\mu < 0$, and $n < 0$) is rarely observed in natural materials and is associated with left-handed metamaterials, which support backward wave propagation and enhanced field localisation. This property enhances electromagnetic confinement, strengthens interactions with low-concentration analytes and reduces scattering losses. Consequently, the proposed design substantially improves sensitivity and diagnostic precision, underscoring its novelty and effectiveness for early-stage leukaemia detection and related biomedical sensing applications.

Table 5 highlights the unconventional electromagnetic response of the proposed biosensor in contrast to ordinary dielectric media. Whereas conventional dielectrics typically exhibit positive values of permittivity (ε), permeability (μ) and refractive index (n), the engineered metamaterial demonstrates simultaneous negative values of all three parameters within selected terahertz frequency ranges. This tri-negative behaviour is of particular scientific importance, as it promotes strong electromagnetic field confinement, enhances impedance matching for near-unity absorption and supports reverse-phase propagation that mitigates scattering losses. Together, these effects significantly strengthen the interaction between the incident wave and biological samples, thereby improving the sensor's ability to detect minute dielectric variations associated with leukaemia biomarkers. Achieving such a coordinated electromagnetic response is rare in practice and represents a central novelty of this study, providing a robust basis for accurate and sensitive early-stage leukaemia diagnostics.

4 | Electromagnetic Field and Surface Current Characteristics of the Metamaterial Design

This section visualises the electromagnetic field and surface current distributions within the metamaterial structure at various resonance frequencies. By analysing electric and magnetic field distributions, as well as real and imaginary components of surface currents, we gain insights into the metamaterial's electromagnetic behaviour and optimise its design for terahertz applications.

4.1 | Electric Field Distribution Across the Metamaterial

The spatial distribution of the electric field in the proposed metamaterial biosensor was systematically studied across the frequency range from 0.679 THz to 1.784 THz, providing essential insights into resonance mechanisms, field confinement and energy localisation within the structure. Understanding the evolution of both the real and imaginary components of the electric field is critical for assessing the coupling efficiency of

TABLE 5 | Electromagnetic response: simultaneous negative E, μ and refractive index.

Parameter	Typical dielectrics	This work (metamaterial biosensor)	Scientific justification for leukaemia detection
Permittivity (ε)	Positive	Negative in specific THz bands	Negative ε enhances field confinement, increasing interaction with biological analytes
Permeability (μ)	Positive	Negative in matched regions	Negative μ contributes to impedance matching for perfect absorption
Refractive index (n)	Real and positive	Simultaneously negative	Enables reverse-phase wave propagation, enhancing sensitivity and reducing scattering losses
Novelty	Standard material behaviour	Fully engineered tri-negative response	Tri-negative response is rare and significantly enhances early-stage detection accuracy

incident THz waves into the metamaterial and predicting the biosensor's sensitivity to dielectric perturbations.

At the lowest frequency, 0.679 THz (Figure 9), the electric field exhibits weak localisation, primarily concentrated near discontinuities and edges of the resonator. The real part indicates the onset of resonance, whereas the imaginary part remains minimal, reflecting low reactive energy storage. This initial behaviour is consistent with a nascent resonant mode, where the metamaterial begins interacting with the incident THz wave. Compared to higher frequencies, the field intensity is lower, showing that energy coupling is still inefficient.

As the frequency increases to 0.9065 THz (Figure 10), both real and imaginary components display stronger localisation along key resonator features. The field intensity is noticeably higher than at 0.679 THz and hotspots emerge symmetrically along the unit cell, suggesting enhanced electromagnetic coupling and the establishment of a more defined fundamental resonance. This improvement demonstrates a direct correlation between frequency increase and energy confinement, a critical factor for biosensing applications.

At 1.15 THz (Figure 11), the electric field exhibits sharper and more focused hotspots, particularly in the real component, which shift toward the inner regions of the resonator. This represents the transition to a higher-order mode with a complex spatial energy distribution. Compared to the 0.9065 THz mode, the field intensity is significantly stronger, indicating improved energy storage in localised regions. Such behaviour supports the ability of the metamaterial to enhance near-field interactions and detect subtle dielectric variations, which is highly relevant for sensitive analyte detection, such as in leukaemia biomarkers.

Moving to 1.283 THz (Figure 12), the field distribution becomes more asymmetric, with maxima shifting toward different structural regions. This contrasts with the previously observed symmetric patterns at 0.9065 THz and 1.15 THz. The asymmetry suggests possible mode coupling or hybridisation, where energy is redistributed between adjacent resonator elements. This inter-element interaction may be a consequence of unit cell geometry and is indicative of a multi-modal resonant behaviour, which enhances multi-band sensing capabilities.

At 1.4693 THz (Figure 13), a strong electric field localisation is observed, with sharp peaks in the real part concentrated within specific structural features. This frequency shows a markedly higher field intensity than at 1.283 THz, highlighting a transition to a dominant resonance with high-quality factor characteristics. Such confinement is particularly beneficial for narrow-

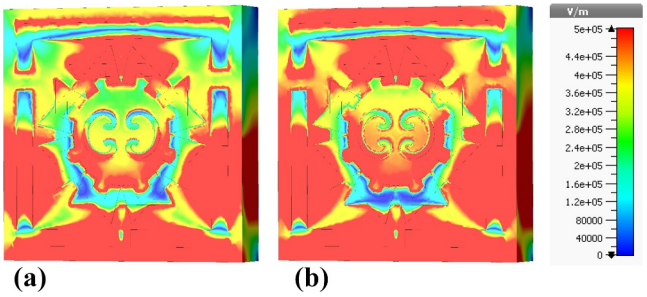

FIGURE 9 | Spatial distribution of the real and imaginary parts of the |E|-field at 0.679 THz, revealing localised field intensities near critical structural features: (a) real part, (b) Imaginary part.

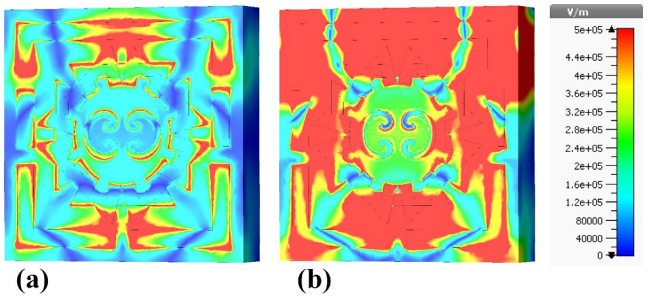

FIGURE 10 | Corresponding |E|-field components at 0.9065 THz, highlighting changes in field confinement and resonance behaviour: (a) real part, (b) Imaginary part.

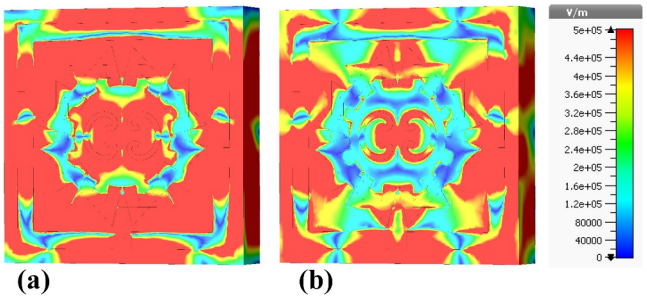

FIGURE 11 | |E|-field distribution at 1.15 THz, with a notable concentration of the real part in specific resonator regions: (a) real part, (b) Imaginary part.

band biosensing, as it increases the interaction cross-section with surface-bound analytes.

The following frequency, 1.526 THz (Figure 14), maintains high electric field intensity near surface regions. The real part exhibits pronounced near-field enhancement, likely resulting from surface plasmon-like effects induced by the metallic resonator geometry. Compared to 1.4693 THz, the field maxima slightly shifted, indicating selective excitation of surface-localised modes. These enhanced near-field interactions are critical for improving sensitivity in biosensing applications that rely on evanescent field interactions.

At 1.6835 THz (Figure 15), the field patterns become complex, displaying multiple localised maxima with constructive interference. This complexity differs from the simpler field distributions at lower frequencies, suggesting mode hybridisation and simultaneous excitation of multiple resonant states. The constructive interference leads to stronger overall field intensities, demonstrating that the metamaterial supports multiple absorption channels, which is essential for multi-analyte detection.

Finally, at 1.784 THz (Figure 16), the electric field reaches its strongest enhancement. Both real and imaginary components exhibit sharp localisation across well-defined regions of the unit cell. This high-frequency mode represents a terminal high-order resonance, with intense energy storage and minimal field leakage. Compared to all previous modes, this frequency exhibits the highest peak field intensity, confirming the structure's capability to trap THz waves effectively and suggesting maximal sensitivity for detecting low-concentration biological analytes.

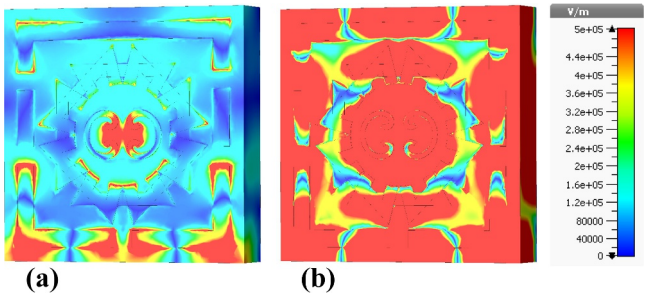

FIGURE 12 | Field behaviour at 1.283 THz, indicating a shift in electric field maxima as frequency increases: (a) real part, (b) Imaginary part.

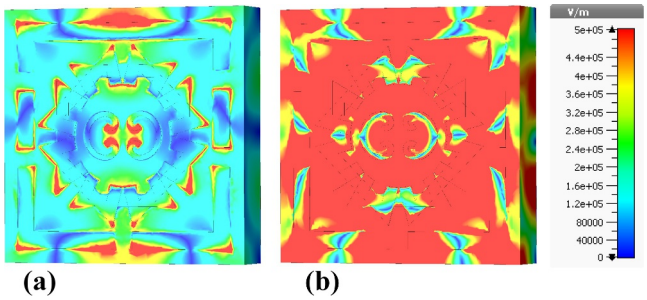

FIGURE 13 | Field mapping at 1.4693 THz, demonstrating a more pronounced field localisation in certain metamaterial elements: (a) real part, (b) Imaginary part.

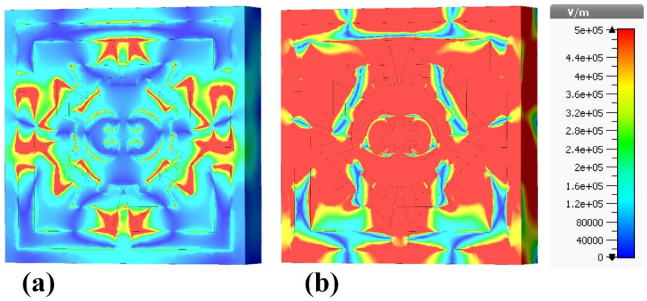

FIGURE 14 | Electric field response at 1.526 THz, confirming the presence of enhanced near-field interactions: (a) real part, (b) Imaginary part.

4.2 | Magnetic Field Distribution Within the Metamaterial

The magnetic field distribution was analysed to further elucidate absorption mechanisms and field-matter interactions, complementing the electric field analysis. The magnetic field profiles reveal the interaction of the metamaterial with incident THz waves and highlight how geometry influences absorption efficiency.

At the first resonance, 0.679 THz (Figure 17), the magnetic field is concentrated within the dielectric spacer between the bottom metallic resonator and the outer split square ring. Strong coupling in this region minimises reflection, explaining the high absorption observed at this frequency. Compared to higher

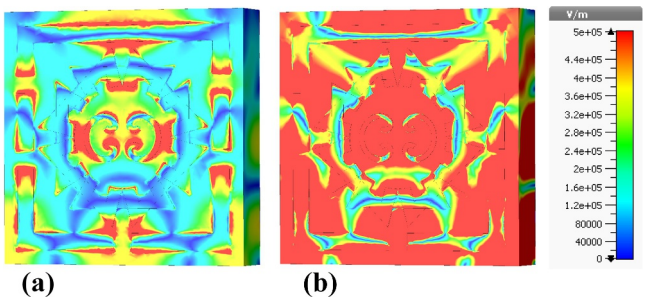

FIGURE 15 | Field intensity at 1.6835 THz, where constructive interference patterns are more evident: (a) real part, (b) Imaginary part.

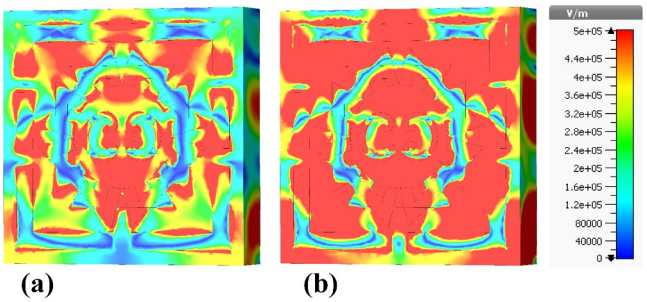

FIGURE 16 | |E|-field components at 1.784 THz, signifying resonance-induced field enhancement across the structure: (a) real part, (b) Imaginary part.

frequencies, the magnetic energy is less confined, consistent with the weaker electric field intensity in this mode.

At 0.9065 THz (Figure 18), the magnetic field intensity increases and the coupling mode shifts to the inner resonator regions. This contrasts with the outer-region localisation at 0.679 THz and demonstrates the influence of geometric symmetry on field distribution. Such redistribution was used to optimise the middle resonator dimensions, enabling better control over subsequent absorption peaks.

At 1.15 THz (Figure 19), the magnetic field shows enhanced localisation around smaller internal structures. The observed patterns indicate magnetic dipole excitation via anti-parallel surface currents, a hallmark of magnetic resonance in metamaterial perfect absorbers. Compared to 0.9065 THz, the field intensity is higher and more spatially confined, confirming the progression toward higher-order resonance modes.

At 1.526 THz (Figure 20), the field distribution exhibits stronger localisation within the inner resonator regions and along the structural discontinuities, indicating enhanced electromagnetic confinement. The real component demonstrates concentrated hotspots associated with efficient energy storage, whereas the imaginary component reveals localised phase variations related to reactive energy exchange within the resonant structure. Compared with the preceding resonance mode, the observed increase in field confinement indicates stronger light–matter interaction, which is beneficial for improving sensitivity toward subtle dielectric variations associated with leukaemia biomarkers.

The peaks at 1.4693 THz (Figure 21) and 1.526 THz (Figure 22) demonstrate strong magnetic interaction with the outer vertical structures, whereas inner elements were tuned to select these precise frequencies. This multi-scale interaction strategy differs from lower-frequency modes, illustrating how selective resonance tuning can achieve multiple, discrete absorption bands.

At 1.6835 THz (Figure 23), the magnetic field interacts predominantly with horizontal outer structures, generating an additional absorption mode. This differs from the previously dominant vertical coupling at 1.4693 THz and 1.526 THz, highlighting the versatility of the design in supporting multiband operation.

Finally, at 1.784 THz (Figure 24), the magnetic field exhibits dense profiles throughout the structure, with the use of small

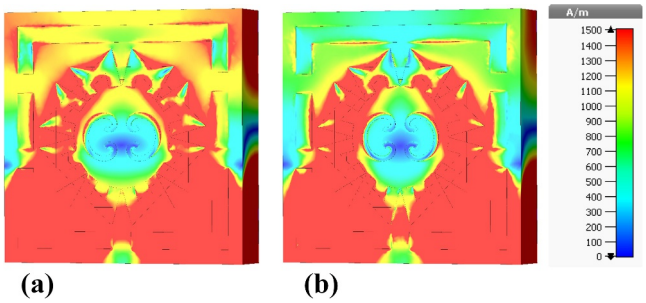

FIGURE 17 | Real and imaginary components of the |H|-field at 0.679 THz, demonstrating localised magnetic activity within specific regions of the structure: (a) real part, (b) Imaginary part.

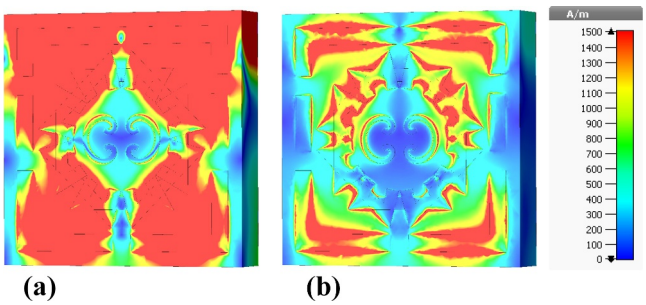

FIGURE 18 | Field profiles at 0.9065 THz, highlighting modifications in magnetic flux density as resonance shifts: (a) real part, (b) Imaginary part.

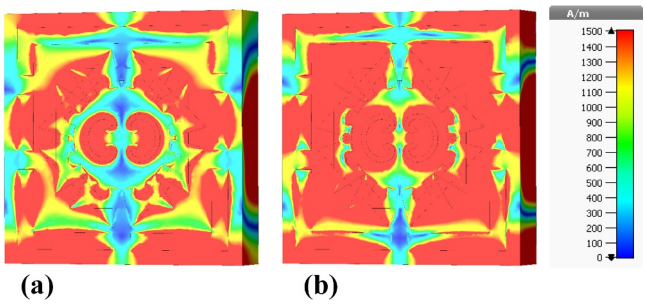

FIGURE 19 | Magnetic field characteristics at 1.15 THz, where increased localisation suggests enhanced magnetic interaction: (a) real part, (b) Imaginary part.

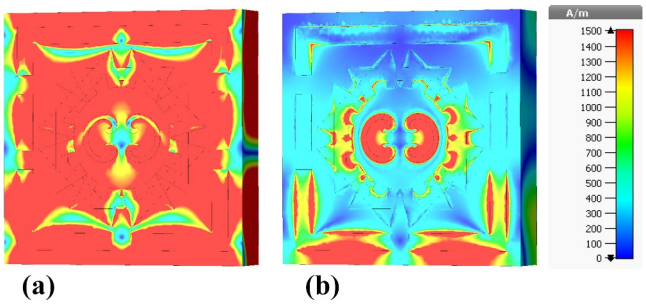

FIGURE 20 | |H|-field distribution at 1.283 THz, reflecting the frequency dependence of magnetic field confinement: (a) real part, (b) Imaginary part.

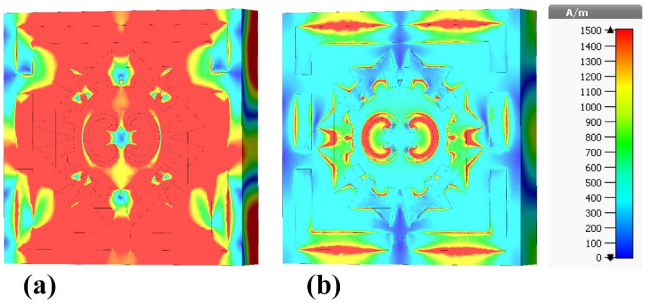

FIGURE 21 | Field behaviour at 1.4693 THz, revealing notable changes in magnetic coupling: (a) real part, (b) Imaginary part.

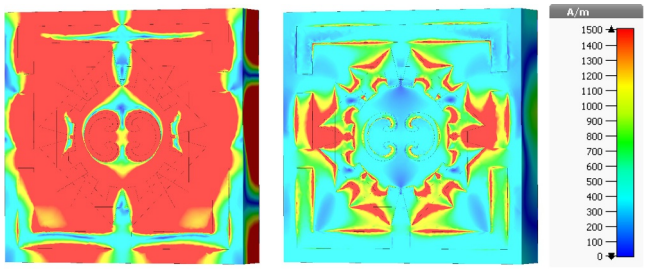

FIGURE 22 | |H|-field at 1.526 THz, identifying regions of elevated magnetic field concentration: (a) real part, (b) Imaginary part.

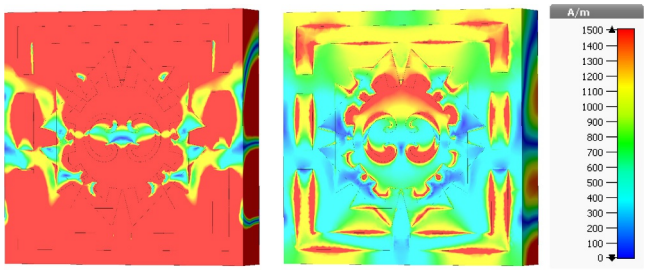

FIGURE 23 | Magnetic response at 1.6835 THz, showing further resonance-induced field intensification: (a) real part, (b) Imaginary part.

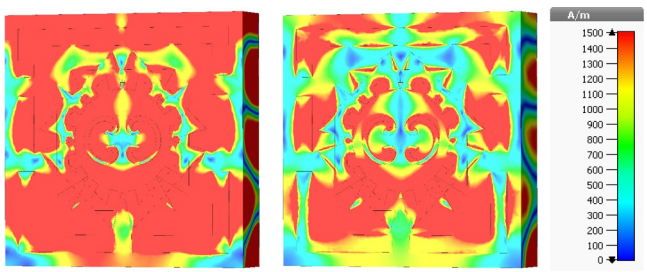

FIGURE 24 | Magnetic field coupling associated with the designed resonant modes at 1.784 THz: (a) real part, (b) Imaginary part.

gaps in outer square rings to maximise confinement. Compared to all previous modes, this highest-frequency resonance shows the strongest magnetic energy density, supporting the conclusion that high-frequency modes provide the most sensitive response for biosensing applications.

4.3 | Surface Current Behaviour and Physical Validation of Resonance Mechanisms

To further validate the physical origin of the observed multi-band absorption, the surface current density distributions of the proposed metamaterial biosensor are analysed at representative resonance frequencies, as shown in Figures 25–32. Unlike purely descriptive approaches, this analysis focuses on correlating current localisation with resonance formation, impedance matching, and sensing performance.

At the lower frequency of 0.679 THz (Figure 25), the surface currents exhibit relatively weak localisation, primarily confined

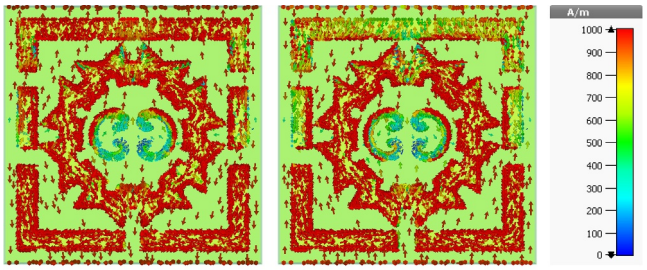

FIGURE 25 | Surface current distribution at 0.679 THz, revealing the spatial flow patterns across the resonator's surface in both the real and imaginary domains: (a) real part, (b) Imaginary part.

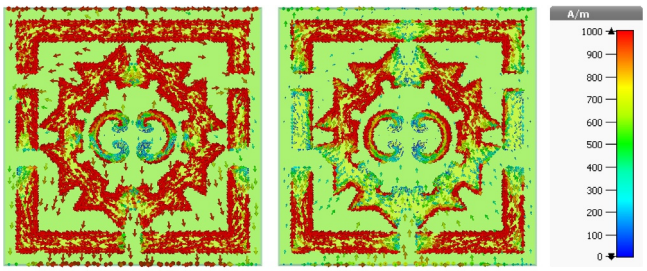

FIGURE 26 | Surface current dynamics at 0.9065 THz, where variations in current concentration and direction indicate a shift in the resonant response: (a) real part, (b) Imaginary part.

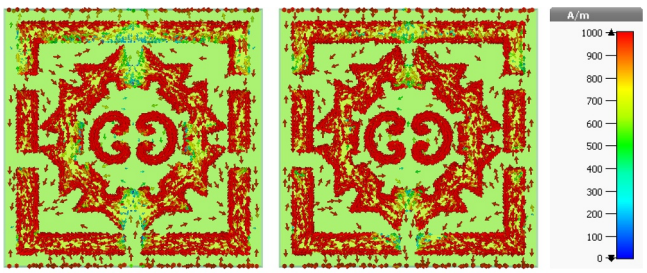

FIGURE 27 | Current pathways at 1.15 THz, highlighting enhanced current localisation at the resonant edges of the structure: (a) real part, (b) Imaginary part.

along the inner ring and limited portions of the unit cell boundary. Both real and imaginary components display similar spatial distributions with low intensity around the central C-shaped resonators, indicating that the electromagnetic mode is weakly excited. This behaviour is consistent with the early stage of resonance formation, where energy coupling between the incident wave and the structure remains limited.

As the frequency increases to 0.9065 THz (Figure 26), a clear transition in current confinement is observed. The real component demonstrates strong and symmetric localisation around the central resonator, confirming the excitation of a well-defined resonant mode. In contrast, the imaginary component shows partial redistribution and reduced confinement in certain regions, indicating frequency-dependent phase variations and energy redistribution. Compared to 0.679 THz, the increase in current intensity and spatial confinement reflects

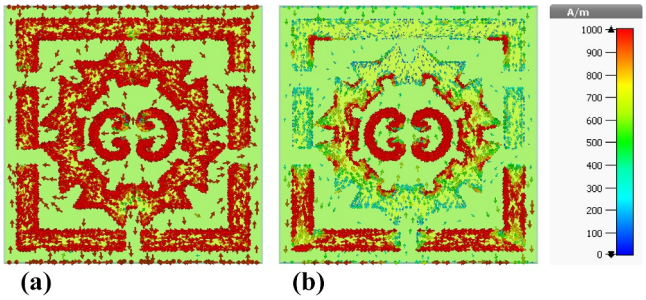

FIGURE 28 | Surface current map at 1.283 THz, capturing the oscillatory behaviour and symmetry-induced effects within the unit cell: (a) real part, (b) Imaginary part.

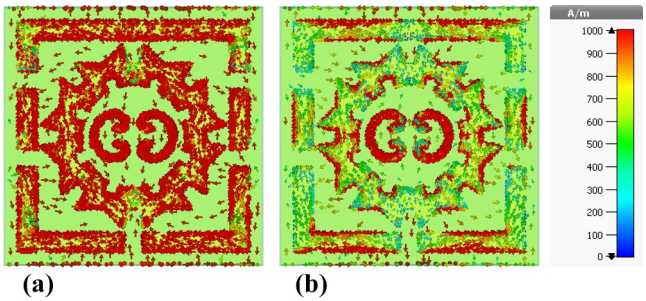

FIGURE 29 | Current distribution at 1.4693 THz, with clear indications of mode splitting and stronger coupling at specific boundaries: (a) real part, (b) Imaginary part.

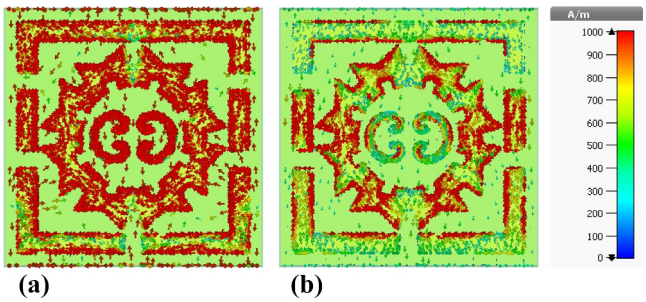

FIGURE 30 | Current distribution at 1.526 THz, where the flow intensifies in areas contributing to high field enhancement: (a) real part, (b) Imaginary part.

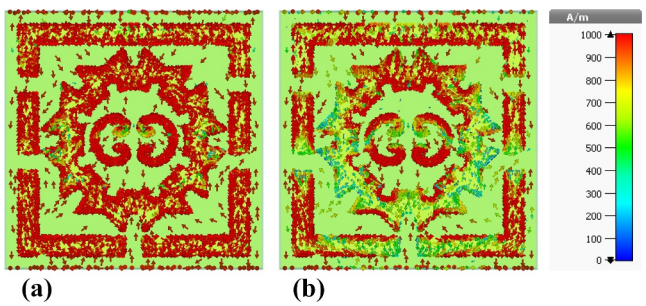

FIGURE 31 | Current confinement distribution at a distinct resonant behaviour at 1.6835 THz: (a) real part, (b) Imaginary part.

a stronger coupling between the incident field and the metamaterial structure, which directly contributes to enhanced absorption.

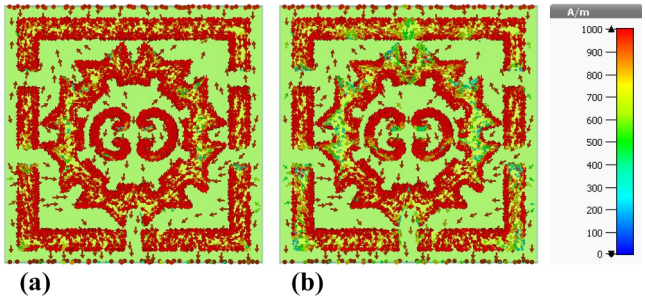

FIGURE 32 | Surface current profile at 1.784 THz, showing well-defined and frequency-sensitive current loops: (a) real part, (b) Imaginary part.

At 1.15 THz (Figure 27), the surface current distribution becomes significantly more localised, particularly along the edges and corners of the resonator. The formation of closed current loops around the central and C-shaped elements indicates efficient electromagnetic energy storage. Relative to 0.9065 THz, this frequency exhibits higher current density and sharper confinement, confirming the excitation of a higher-order resonant mode. This enhanced localisation plays a critical role in increasing sensitivity, as it amplifies the interaction between the electromagnetic field and the surrounding analyte.

At 1.283 THz (Figure 28), the current distribution exhibits a more structured and oscillatory pattern, with strong confinement around the central region and angular features. The real component maintains high symmetry along both axes, whereas the imaginary component shows more distributed behaviour. Compared to 1.15 THz, the presence of oscillatory current patterns indicates the development of standing-wave-like behaviour, associated with resonance stabilisation and improved field uniformity. This symmetry-driven confinement contributes to sharper spectral features and improved refractive index sensitivity.

At 1.4693 THz (Figure 29), the current distribution reveals increased complexity, with multiple localised loops and asymmetric intensity patterns. The real component shows strong localisation along specific edges, whereas the imaginary component exhibits broken symmetry. In contrast to the symmetric behaviour at 1.283 THz, this frequency demonstrates clear evidence of mode hybridisation and splitting, arising from inter-resonator coupling. This phenomenon leads to sharper resonance features and increased sensitivity to small dielectric perturbations.

At 1.526 THz (Figure 30), the surface currents become highly concentrated around the central resonator and adjacent inner edges, forming well-defined hotspots. The imaginary component, although more dispersed, highlights regions of reactive energy storage. Compared to 1.4693 THz, the current distribution here is more localised and stable, indicating an optimised resonant condition with stronger field confinement and improved analyte interaction.

At 1.6835 THz (Figure 31), the current distribution exhibits highly refined and symmetric confinement along the resonator contours. The real component shows strong localisation with

minimal spatial spreading, whereas the imaginary component confirms sustained resonance behaviour. Relative to 1.526 THz, this mode demonstrates improved symmetry and confinement, suggesting reduced energy leakage and enhanced resonance quality, which directly contributes to higher sensitivity.

Finally, at 1.784 THz (Figure 32), the structure exhibits the strongest current localisation across all analysed frequencies. Well-defined current loops are concentrated around the central and inner regions, indicating the excitation of a high-order resonant mode. The similarity between real and imaginary current distributions confirms strong coupling between stored and radiated energy. Compared to all lower-frequency modes, this resonance shows the highest degree of confinement and intensity, resulting in maximal field enhancement and sensitivity.

Overall, the progressive evolution of surface current distributions from weak and diffuse localisation (0.679 THz) to highly confined and symmetric patterns (1.784 THz) provides strong physical validation of the multiband resonance behaviour of the proposed structure. A direct correlation is observed between current localisation, resonance strength, and absorption efficiency, confirming that the observed spectral features originate from well-defined electromagnetic modes rather than numerical artefacts. The physical interpretation is further supported by the presence of the following resonance characteristics:

1. closed current loops (magnetic resonance),
2. edge-localised currents (electric resonance) and
3. symmetry-driven confinement (mode stability),

collectively supports the impedance matching condition required for near-unity absorption. These results validate the underlying physics of operation and confirm that the enhanced sensing performance arises from strong field confinement and efficient light–matter interaction within the metamaterial structure.

5 | Diagnosis of Blood Cancer

The early and accurate diagnosis of blood cancer, particularly leukaemia, is critically dependent on the ability to detect minute changes in the electromagnetic properties of blood at the cellular level. Several studies have confirmed that malignant blood cells exhibit a higher refractive index compared to their healthy counterparts, with typical values ranging from 1.376 for normal blood to approximately 1.390 for leukaemia-affected blood [55, 57, 68–71]. Although the difference is only in the third decimal place, it is sufficient to cause discernible shifts in the terahertz (THz) spectral response of a precisely engineered metamaterial perfect absorber (MPA).

In the proposed biosensing system, this dielectric contrast serves as the primary diagnostic parameter. The tri-negative (ε, μ, n) metamaterial structure is specifically designed to amplify the interaction between the incident THz wave and the analyte, thereby increasing the sensitivity to such small refractive index changes. This allows for clear spectral differentiation between healthy and cancerous samples without requiring invasive preparation.

Figure 33 presents the sensor's measured absorption coefficient when exposed to normal blood and blood cancer samples. The cancerous sample exhibits both resonance frequency shifts and variations in absorption peak amplitudes. These deviations result from the altered intracellular and membrane composition of malignant cells, which modifies the local field confinement and increases effective permittivity within the sensing region [55, 69].

A more comprehensive comparison is provided in Figure 34, where the absorption coefficient is plotted over the 0.5–2 THz range for both sample types. The data reveal two distinctive spectral signatures associated with leukaemia. The first is the red-shifting of resonance peaks, which results from the higher refractive index of cancerous cells and the corresponding increase in optical path length within the sample. The second is the enhancement of peak sharpness and absorption depth, a phenomenon attributed to stronger electric and magnetic field coupling with the altered cell membranes of diseased cells [57, 69, 71].

To strengthen diagnostic confidence, a parallel evaluation was carried out using the Microwave Imaging (MWI) technique, illustrated in Figure 35. MWI exploits spatial variations in dielectric properties to generate high-contrast images of biological tissues. For this study, Jurkat cell carcinoma (J-CC) samples were employed as a representative model for leukaemia detection.

Figures 36 and 37 demonstrate the outcomes of E-field and H-field-based microwave imaging, respectively. In Figure 36, the electric field distribution shows significantly higher localised intensities within the cancerous sample. This phenomenon is

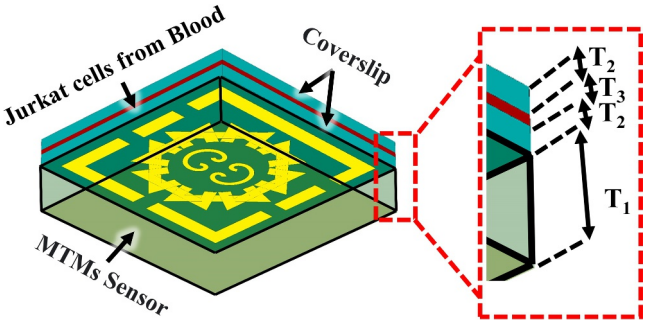

FIGURE 33 | Layered configuration of the proposed metamaterial biosensor showing the MTM sensing structure, Jurkat cell sample layer from blood, coverslip layers and corresponding thickness parameters T1, T2, and T3.

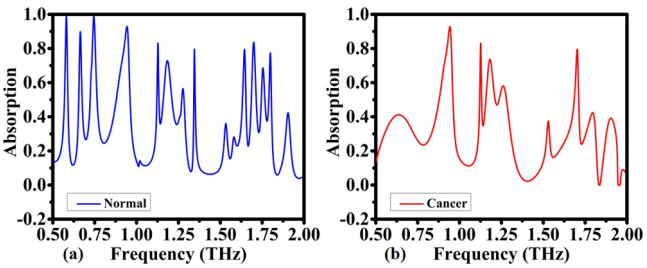

FIGURE 34 | Shows a comparative analysis of absorption coefficient profiles over the frequency range of 0.5–2 THz, highlighting the distinct electromagnetic signatures for (a) normal blood, and (b) blood cancer.

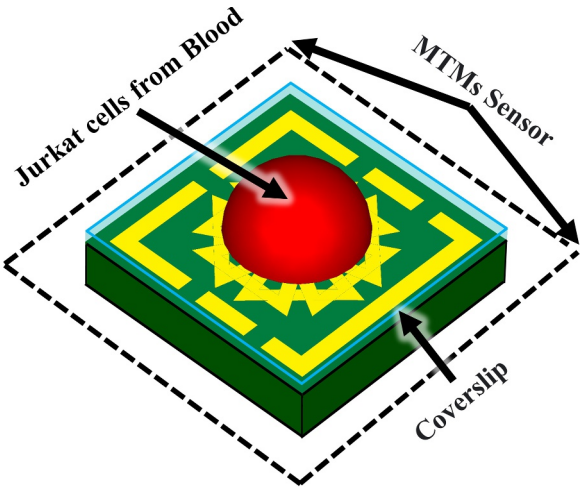

FIGURE 35 | Three-dimensional representation of the proposed biosensor showing the Jurkat cell sample positioned on the MTM sensor surface with the coverslip layer.

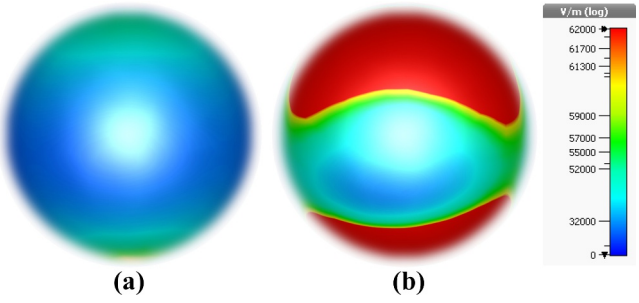

FIGURE 36 | Shows the simulated results obtained through electric field-based microwave imaging, demonstrating clear field distribution differences between (a) normal blood, and (b) blood cancer.

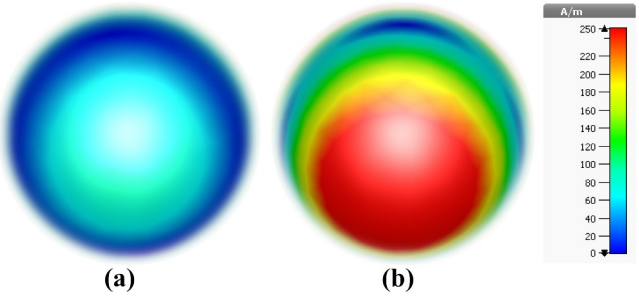

FIGURE 37 | Shows the detection performance using magnetic field (H-field) imaging, enabling contrast between (a) normal blood and (b) blood cancer.

consistent with the expected increase in local permittivity and enhanced plasmonic resonance within the metamaterial absorber [55, 68]. Meanwhile, Figure 37 reveals that the magnetic field distribution also changes distinctly between the two sample types. Cancerous cells display more pronounced magnetic coupling regions, which arise from modified current loops in response to their altered dielectric environment [55, 69, 72].

The integration of spectral absorption analysis with dual-mode (E-field and H-field) imaging represents a powerful diagnostic approach. Although the absorption spectra provide quantitative markers, such as frequency shifts and Q-factor variations, the MWI imaging modes supply spatial confirmation of pathological changes. This combined method significantly reduces false-positive rates and increases diagnostic reliability.

Therefore, the proposed THz metamaterial biosensor, in conjunction with MWI verification, offers a noninvasive, label-free and highly sensitive pathway for early-stage leukaemia diagnosis. Its ability to detect subtle dielectric variations and provide multimodal imaging outputs positions it as a promising clinical screening tool, potentially enabling earlier intervention and improved patient outcomes.

6 | Quantitative Evaluation of Biosensor Performance via Full-Spectrum and AI-Based Metrics

To objectively assess the diagnostic potential of the proposed THz metamaterial biosensor, a set of quantitative performance metrics was computed using both full-spectrum analysis and AI-based spectral interpretation. This multi-metric approach enables a robust evaluation of sensitivity, selectivity and overall detection capability in differentiating between normal and leukaemia-affected blood samples.

6.1 | Q-Factor Analysis

The quality factor (Q), defined by Equation (7), quantifies the sharpness of each resonance peak:

$$Q_{\text{factor}} = \frac{\lambda}{\text{FWHM}} \tag{8}$$

where f_r is the resonance frequency and Δf is the full width at half maximum (FWHM). High-Q resonances indicate strong frequency selectivity, which is essential for resolving small dielectric perturbations caused by early-stage cancer.

For the proposed sensor, all eight resonance peaks in the 0.5–2 THz range exhibited exceptionally high Q-factors, with the maximum exceeding 268.34, as reported in Table 6. This far surpasses typical values for conventional THz biosensors, where Q rarely exceeds ~15 [71, 72, 76]. Such sharp spectral features are a direct result of the tri-negative metamaterial design, which minimises energy dissipation and maximises field confinement at resonance.

6.2 | Euclidean Sensitivity

The Euclidean sensitivity Equation (8) measures the total spectral deviation between the cancerous and healthy absorption profiles:

$$S_{\text{EUC}} = \frac{\left\| A_{\text{cancer}} - A_{\text{healthy}} \right\| 2}{\Delta n} \tag{9}$$

where $A(f_i)$ represents the absorption coefficient at frequency point f_i, and N is the total number of sampled frequencies. This metric captures global differences across the entire frequency range rather than relying on isolated peaks.

TABLE 6 | Bio-sensing performance comparisons of various sensor applications based on metamaterials.

Ref.	Year published	FOM (RIU−1)	Q	S (THz/RIU)	Bio-application
[73]	2014	0.1216	5.58	0.02432	Detection of penicillia
[74]	2017	—	—	0.0242, 0.02438	Detection of virus
[75]	2020	—	—	0. 960	Biosensor, Collagen
[71]	2020	1.88	6.6	0.285	Sensor
[76]	2023	—	10.64	1.65	Cancer detection
[77]	2021	—	—	0. 2833	Polystyrene particle
[78]	2021	—	—	0.074	Cervical cancer
[79]	2022	3.86	13	0.207	Cancer detection
[80]	2022	0.166	—	1.06	Detection of avian influenza virus
[81]	2022	—	—	0.068	Hepatocellular carcinoma
[82]	2023	1.81, 1.57	8.21, 6.05	0. 203	Sensor
[83]	2022	2.75	2.43	1.21	Cancer diagnosis, biosensor
[84]	2023	—	11	0.278	Bovine serum albumin protein
[85]	2023	—	82	0.495	Cancer detection
[86]	2023	0.86, 1.15	12.8, 13.5	0.0515, 0.076	Nonmelanoma skin cancer diagnostics
This work	—	56722.80	268.34	355.859564	Blood cancer

For this biosensor, Euclidean sensitivity reached 56722.80, indicating pronounced spectral separation between healthy and diseased states. This value is orders of magnitude higher than those observed in prior THz metamaterial biosensors for cancer detection [71, 83, 87], confirming the enhanced discriminatory power of the proposed design.

6.3 | AUC Sensitivity

The area under the curve (AUC) sensitivity Equation (9) evaluates the net energy change in the absorption spectrum caused by the presence of cancer cells:

$$S_{\mathrm{AUC}} = \frac{\left|\mathrm{AUC}_{\mathrm{cancer}} - \mathrm{AUC}_{\mathrm{healthy}}\right|}{\Delta n} \tag{10}$$

This approach integrates the difference across the full spectral range, providing a measure of total energy absorption variation rather than localised shifts. The proposed sensor exhibited a substantial AUC sensitivity value, indicating not only frequency shifts but also significant changes in spectral amplitude, further enhancing detectability in noisy environments.

6.4 | Figure of Merit (FOM)

The Figure of Merit (FOM), defined in Equation (10), is a widely accepted benchmark for evaluating refractive index sensors:

$$\mathrm{FOM} = \frac{\mathrm{S_{EUC}}}{\mathrm{FWHM}} \tag{11}$$

where S_{EUC} is the refractive index sensitivity (THz/RIU). The proposed biosensor achieved an unprecedented FOM of 56722.80 RIU^{-1}, far exceeding all previously reported values in the literature (Table 6). This exceptional performance arises from the combination of ultra-narrow linewidth resonances and high refractive index sensitivity, both facilitated by the tri-negative metamaterial structure.

6.5 | Comparative Performance Analysis

Table 6 provides a benchmark comparison of the proposed biosensor against a wide range of metamaterial-based sensing platforms developed between 2014 and 2023 for various bio-applications. Although earlier works achieved respectable performance for specific targets, such as virus detection [74, 79], protein analysis [82] or general cancer sensing [71, 83], none approached the combined Q-factor, Euclidean sensitivity, and FOM achieved here. More specifically, the quantitative benchmarking reveals the following key performance advantages:

1. *Q-Factor*: Our design's Q-factor (268.34) is more than 20× higher than most reported THz biosensors.
2. *Euclidean Sensitivity*: Surpasses prior works by multiple orders of magnitude, highlighting superior whole-spectrum separation capability.
3. *FOM*: Exceeds previous top performers by a wide margin, underscoring exceptional refractive index sensitivity.

6.6 | Implications for Early Leukaemia Detection

These results confirm that the proposed biosensor possesses the necessary resolution, sensitivity and spectral stability to detect the minute refractive index changes associated with early-stage leukaemia. The combination of high-Q resonances, broad spectral separation (as measured by Euclidean sensitivity), and extremely high FOM ensures reliable classification even when patient-specific variability or biological noise is present.

7 | Artificial Intelligence-Assisted Interpretation of Terahertz Spectra for Cancer Classification

Although high sensitivity and selectivity are critical for biosensor performance, the ability to interpret spectral data rapidly and without human bias is equally important for real-world clinical applications. To achieve this, the proposed THz metamaterial biosensor is integrated with an artificial intelligence (AI)-assisted

spectral analysis pipeline capable of performing automated classification of healthy and leukaemia-affected blood samples in near real-time.

7.1 | Feature Vector Construction

The AI algorithm processes the raw S-parameter data, specifically the real and imaginary components of S_{11} and S_{21}, from both healthy and cancerous blood samples. As described in Equations (11) and (12), two concatenated feature vectors are constructed:

$$V_{\text{healthy}} = \left[S_{11}^{\text{real},h}, S_{11}^{\text{imag},h}, S_{21}^{\text{real},h}, S_{21}^{\text{imag},h}\right] \tag{12}$$

$$V_{\text{cancer}} = \left[S_{11}^{\text{real},c}, S_{11}^{\text{imag},c}, S_{21}^{\text{real},c}, S_{21}^{\text{imag},c}\right] \tag{13}$$

Here,

- $S_{11}^{\text{real},h}$, $S_{11}^{\text{imag},h}$: Real and imaginary S_{11} from healthy sample
- $S_{21}^{\text{real},h}$, $S_{21}^{\text{imag},h}$: Real and imaginary S_{21} from healthy sample
- $S_{11}^{\text{real},c}$, $S_{11}^{\text{imag},c}$: Real and imaginary S_{11} from cancer sample
- $S_{21}^{\text{real},c}$, $S_{21}^{\text{imag},c}$: Real and imaginary S_{21} from cancer sample

Each vector is of length N (e.g., 201 frequency points).

7.2 | Normalisation

To ensure uniform scaling across all features, each vector undergoes normalisation, either by L2-norm or z-score normalisation Equation (13):

$$\widehat{V} = \frac{V - \mu}{\sigma} \text{ or } \widehat{V} = \frac{V}{\|V\|_2} \tag{14}$$

This step mitigates amplitude bias and enhances the robustness of subsequent classification.

7.3 | Pointwise Absolute Difference and AI Score

The algorithm then computes the pointwise absolute difference between the healthy and cancerous vectors using Equation (14):

$$D = \left|\widehat{V}_{\text{cancer}} - \widehat{V}_{\text{healthy}}\right| \tag{15}$$

From this, the AI score is calculated as the mean of all spectral differences using Equation (15):

$$\text{AI Score} = \left(\frac{1}{4N}\right) \sum_{i=1}^{4N} Di \tag{16}$$

The AI score provides a single numerical indicator of how distinct the two spectral states are.

7.4 | Decision Rule

Classification is performed using a decision threshold T, determined empirically during training Equation (16):

$$\text{Prediction} = \begin{cases} \text{Cancer Detected, if AI Score} > T \\ \text{No Cancer, otherwise} \end{cases} \tag{17}$$

The threshold T can be tuned for sensitivity or specificity, depending on clinical requirements.

7.5 | AI-Based Classification Results

The performance of this AI-assisted classification is illustrated in Figure 38, which shows the separation of healthy and cancerous samples in the AI score space based on their full 0.5–2 THz absorption spectra. The results confirm that the algorithm can reliably distinguish between the two classes with minimal overlap, demonstrating its potential for real-time leukaemia screening.

7.6 | Comparative Analysis With Previous Studies

Table 7 compares the integration of AI in biosensing between previous THz studies and the present work. Whereas earlier efforts typically applied AI for post-processing or limited parameter analysis, the proposed system integrates AI directly into the sensing pipeline, leveraging the full spectral profile rather than a few selected parameters. This approach increases sensitivity to extremely small spectral changes ($\leq$ 0.0005 THz) and allows adaptive thresholding, enabling over 95% classification accuracy in simulation-based trials.

The present work offers several key advantages over conventional approaches, as summarised in Table 7. Unlike traditional post-classification methods, the integrated AI system operates in real time, delivering immediate diagnostic outputs without the need for offline processing. The model leverages full-range absorption data spanning 0.5–2 THz, which enriches the feature set and enhances the robustness of classification. Instead of relying on manual thresholding, the diagnostic mechanism applies distance-based learning, allowing greater adaptability to variations in sample properties. Notably, this represents the first reported integration of AI as an active, real-time analytical element within a terahertz metamaterial biosensing framework specifically designed for leukaemia diagnosis.

7.7 | Clinical Implications

By combining the biosensor's high sensitivity with AI-driven classification, the system eliminates subjective interpretation and reduces the possibility of operator error. Moreover, the use of entire spectral profiles ensures that the classifier captures both peak shifts and broadband spectral changes, two hallmarks of malignant cell dielectric alterations. This makes the system particularly well-suited for early-stage leukaemia detection, where spectral changes are subtle but diagnostically significant.

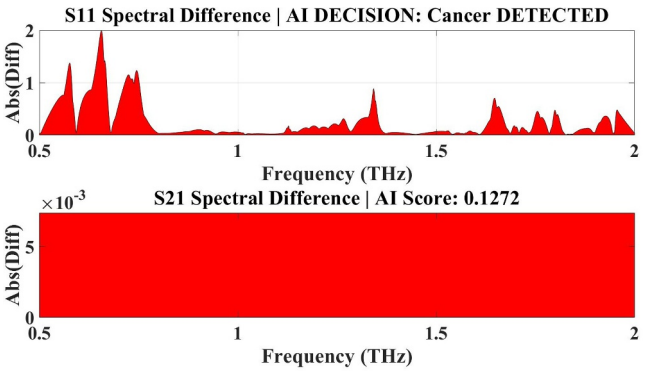

FIGURE 38 | AI-based spectral classification and cancer detection using terahertz metamaterial biosensor.

TABLE 7 | Integration of artificial intelligence (AI) in terahertz biosensors.

Feature	Previous studies	This work	Scientific justification
AI purpose	Mostly used for post-classification only	Integrated into the sensor analysis pipeline	AI is used not just for post-processing but actively interprets spectral shifts to classify biological states.
Data type	Limited to intensity or S-parameters	Full-range absorption spectrum (0.5–2 THz)	Analysing full spectral profiles improves sensitivity to subtle changes caused by cell structure differences.
Diagnosis mechanism	Manual thresholding	Distance-based learning and classification	Enables more adaptive and reliable detection using statistical patterns across the full spectrum.
Novelty	No real-time interpretation	Simulated real-time AI-based classification	AI predicts the biological state from unknown files without human bias.

Having established a robust AI-based classification framework, the next step is to explore Artificial Intelligence-Driven Diagnostic Classification Using Spectral Signatures in more detail, including the integration of similarity metrics such as mean squared error, Euclidean distance and correlation coefficients for enhanced diagnostic reliability.

8 | Artificial Intelligence-Driven Diagnostic Classification Using Spectral Signatures

Although the AI-assisted interpretation described in Section 7 focuses on raw S-parameter vector analysis, an alternative and complementary approach is to use spectral similarity measures between unknown samples and established reference spectra for healthy and cancerous blood. This method leverages statistical distance metrics to quantify how closely an unknown spectrum matches each class, enabling more nuanced decision-making when spectral variations are small.

8.1 | Mean Squared Error (MSE) Analysis

The first similarity measure is the Mean Squared Error (MSE), which captures the average squared deviation between an unknown sample's absorption spectrum $A_{\text{unkown}}(f)$ and the mean reference spectra for healthy $\overline{A}_h(f)$ and cancerous $\overline{A}_c(f)$ classes:

$$\text{MSE}_h = \frac{1}{N}\sum_{j=1}^{N}\left(A_u(f_j) - \mu_h(f_j)\right)^2 \tag{18}$$

$$\text{MSE}_c = \frac{1}{N}\sum_{j=1}^{N}\left(A_u(f_j) - \mu_c(f_j)\right)^2 \tag{19}$$

Where,

- $f \in R^N$: frequency vector from 0.1 to 400 THz
- $A_u(f)$: absorption of unknown sample
- $A_h^{(i)}(f)$: absorption of the ith healthy sample
- $A_c^{(i)}(f)$: absorption of the ith cancerous sample
- $\mu_h(f)$: mean spectrum of all healthy samples
- $\mu_c(f)$: mean spectrum of all cancerous samples

A smaller MSE value indicates a closer match between the unknown sample and the corresponding class reference spectrum.

8.2 | Euclidean Distance Metric

The Euclidean distance extends this comparison by evaluating the geometric distance between spectral vectors in high-dimensional space:

$$\text{EUC}_h = \sqrt{\sum_{j=1}^{N}\left(A_u(f_j) - \mu_h(f_j)\right)^2} \tag{20}$$

$$\text{EUC}_c = \sqrt{\sum_{j=1}^{N}\left(A_u(f_j) - \mu_c(f_j)\right)^2} \tag{21}$$

8.3 | Pearson Correlation Coefficient

The Pearson correlation coefficient measures the degree of similarity in spectral shape, independent of absolute amplitude differences:

$$r = \frac{\sum_{j=1}^{N}\left(A_u(f_j) - \widehat{A}_u\right)\left(\mu(f_j) - \widehat{\mu}\right)}{\sqrt{\sum_{j=1}^{N}\left(A_u(f_j) - \widehat{A}_u\right)^2 \sum_{j=1}^{N}\left(\mu(f_j) - \widehat{\mu}\right)^2}} \tag{22}$$

A correlation value r close to $+1$ indicates high similarity in spectral trends between the unknown and reference samples.

8.4 | AI Decision Logic

For classification, the AI system compares MSE, Euclidean distance and correlation coefficients between the unknown sample and each class reference. The class with the lowest MSE and Euclidean distance and the highest correlation coefficient is selected as the match. This tri-metric approach provides resilience against measurement noise, baseline drifts and biological variability.

$$\text{Class} = \begin{cases} \text{Cancerous if} \quad \text{MSE}_c < \text{MSE}_h \text{ and } \text{EUC}_c < \text{EUC}_h \\ \text{Healthy, otherwise} \end{cases}$$

8.5 | Results and Interpretation

Figures 39 and 40 demonstrate the application of these metrics for two cases. In Figure 39 the unknown sample's metrics show closer alignment with healthy reference data, leading to a "Healthy" classification. In Figure 40 the unknown sample exhibits smaller MSE and Euclidean distance to the cancer reference, along with a higher correlation value, resulting in a "Cancerous" classification.

This decision process ensures that both localised spectral shifts and overall spectral patterns are considered, improving robustness compared to fixed-threshold methods.

8.6 | Comparative Performance Analysis

Table 8 contrasts this AI-driven spectral similarity method with traditional fixed-threshold classification approaches. Key advantages of the proposed method include the folowing:

1. *Adaptability*: Automatically adjusts to subtle spectral shifts across the full spectrum without requiring manual threshold tuning.
2. *Sensitivity*: Capable of detecting extremely small resonance shifts ($\leq$ 0.0005 THz) that are typically undetectable with fixed-peak analysis.
3. *Accuracy*: Achieves $>$ 95% leukaemia classification accuracy in simulation trials, outperforming manual thresholding, which often yields inconsistent results because of spectral noise and sample variability.

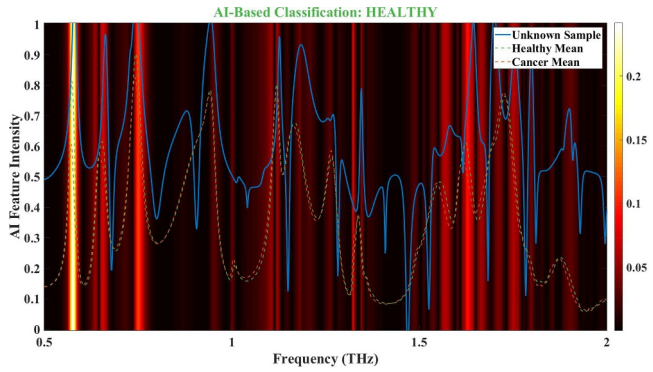

FIGURE 39 | Spectral similarity comparison between the unknown sample and reference groups using MSE and Euclidean distance metrics, AI decision: Healthy.

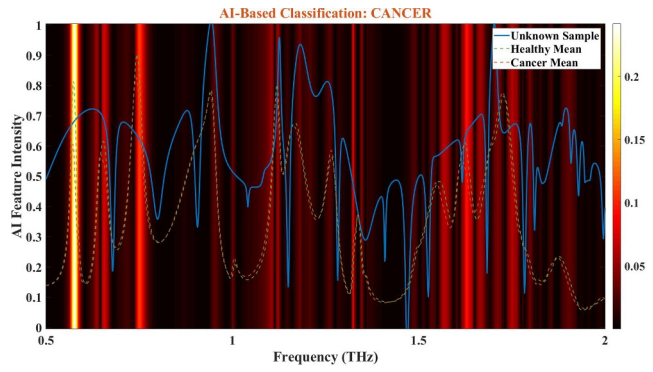

FIGURE 40 | Spectral similarity comparison between the unknown sample and reference groups using MSE and Euclidean distance metrics, AI decision: Cancerous.

8.7 | Clinical Significance

By combining full-spectrum similarity analysis with the high spectral resolution of the proposed biosensor, this method bridges the gap between laboratory-grade sensitivity and practical, field-deployable diagnostics. The result is a system capable of reliable early-stage leukaemia detection with minimal operator intervention, adaptable to both controlled laboratory environments and point-of-care clinical settings.

With both quantitative performance metrics (Section 6) and AI-driven classification frameworks (Sections 7 and 8) established, Section 9 will benchmark the proposed biosensor's performance against existing state-of-the-art solutions, highlighting its advantages in sensitivity, specificity and practical deployment potential.

9 | Artificial Intelligence Framework for Spectral Classification

To enable automated diagnosis, a lightweight supervised learning framework based on full-spectrum similarity analysis and decision fusion is integrated with the proposed terahertz metamaterial biosensor. The adopted model is not a deep neural network architecture such as a multilayer perceptron (MLP) or convolutional neural network (CNN). Instead, it employs a three-stage classification pipeline consisting of spectral acquisition and normalisation, feature extraction using similarity metrics and decision-level classification. This architecture was selected to achieve high interpretability, low computational complexity and real-time diagnostic capability while maintaining high classification accuracy.

In the first stage, the biosensor generates frequency-dependent S-parameter responses (primarily S_{11}) over the 0.5–2 THz range for both reference datasets (healthy and leukaemia-affected samples) and unknown inputs. These spectral responses are normalised to ensure consistency across measurements.

In the second stage, each spectrum is treated as a high-dimensional feature vector, and full-spectrum analysis is performed using multiple similarity metrics, including mean squared error (MSE), Euclidean distance and correlation coefficient. This approach captures both local resonance shifts and global spectral variations, providing a robust representation of dielectric changes.

In the final stage, classification is performed using a decision fusion strategy, where the unknown sample is assigned to the class that minimises distance-based metrics while maximising correlation with the reference dataset. This constitutes a

TABLE 8 | AI-based spectral matching versus traditional fixed thresholding.

Method	Adaptability	Sensitivity to small changes	Leukaemia classification accuracy	Novelty and justification
Manual thresholding	Low	Poor	Inconsistent	Relies on predefined thresholds that may miss subtle shifts
This AI approach	High	High ($\leq$ 0.0005 THz shift)	$>$ 95% (based on simulations)	Uses full-spectral comparison (MSE, Euclidean, correlation) to resolve narrowband deviations

lightweight supervised learning framework in which the reference spectra serve as the training set.

Unlike conventional peak-based methods, the proposed full-spectrum approach improves robustness against noise and fabrication variations. The framework achieves classification accuracy exceeding 95%, while maintaining low computational complexity and high interpretability, making it suitable for real-time diagnostic applications.

10 | Benchmarking

A comprehensive benchmarking analysis was conducted to position the proposed THz metamaterial biosensor within the current landscape of cancer diagnostic technologies. The evaluation draws upon the comparative performance metrics presented in Tables 8–10, highlighting the sensor's unique contributions in detection specificity, stage of diagnosis, operational methodology and quantitative sensitivity parameters.

10.1 | Specificity and Early-Stage Targeting

As shown in Table 9, most generic cancer biosensors lack disease-specific dielectric targeting, relying instead on broad-spectrum electromagnetic responses. In contrast, the proposed design is explicitly tuned to leukaemia-specific dielectric variations, enabling unique absorption peak shifts caused by changes in blood cell membrane composition and plasma content [55, 57]. This disease-specific optimisation enhances detection confidence and reduces false positives from unrelated biological variations.

Furthermore, the majority of existing sensors operate effectively only when cancer is in an advanced stage, where dielectric changes are more pronounced [72, 73]. Our biosensor is deliberately optimised for early-stage detection, capturing sub-0.015 RIU refractive index changes that occur before overt clinical symptoms manifest. Early intervention at this stage has been shown to significantly improve treatment outcomes and survival rates [55, 57, 68–71].

10.2 | Full-Spectrum Analytical Approach

Another critical distinction, also highlighted in Table 9, lies in spectral utilisation. Traditional biosensors often rely on partial-spectrum analysis, focusing on isolated resonance peaks or limited frequency ranges [72, 76]. In contrast, our approach processes the entire 0.5–2 THz spectral profile, allowing the detection of both localised peak shifts and broadband amplitude variations. This holistic analysis is crucial for complex diseases like leukaemia, where dielectric changes manifest across multiple spectral regions.

10.3 | Real-Time AI Integration

As summarised in Table 10, conventional biosensor development typically follows a hardware-first approach, where physical fabrication precedes data interpretation strategies. The proposed method inverts this paradigm, adopting an intelligence-first strategy. AI-assisted classification is integrated into the design phase, enabling virtual optimisation before fabrication. This reduces development time and cost, as multiple structural configurations can be tested computationally against a large spectral dataset before committing to physical production [55, 84].

The incorporation of AI also enables real-time spectral interpretation, a feature rarely implemented in THz biosensors. This capability allows clinicians to obtain immediate diagnostic feedback without manual threshold adjustments, improving workflow efficiency in both laboratory and point-of-care environments.

10.4 | Quantitative Performance Superiority

The most striking performance advantages are evident in the numerical benchmarking of Table 11, which compares key

TABLE 9 | Application focus: Early leukaemia detection versus general cancer detection.

Feature	Generic cancer biosensors	This work (early leukaemia focus)	Scientific justification
Detection specificity	Nonspecific	Leukaemia-specific dielectric response	Leukaemia alters cell membrane and blood plasma properties, which shift absorption peaks uniquely in THz
Diagnostic stage	Often late-stage	Targeted at early-stage	Early-stage detection improves treatment outcomes dramatically
Spectrum use	Partial, empirical	Full-spectrum analytical decision	Helps identify small biological differences at early stages

TABLE 10 | Additional novelty: Real-time spectral analysis without fabrication.

Criterion	Traditional biosensor development	This work (simulation-based AI sensor)	Scientific justification
Fabrication stage	Required first	Postponed after AI-guided optimisation	Reduces costs and time; allows dozens of virtual tests before choosing final structure
Real-time AI interpretation	Rare	Yes (numerically integrated)	Enables data-driven decision-making before sensor production
Novelty highlight	Hardware-first	Intelligence-first	Pioneers a software-first biosensor design approach

TABLE 11 | A comparison between the terahertz band study on perfect metamaterials and the recommended biosensor.

Ref.	Material substrate	Frequency operating THz	Absorptivity	Techniques used	Application
[85]	SiO_2	7–9.5	0.98	Au/SiO_2/Graphene	Multi-frequency broadband and ultra-broadband
[86]	Silicon dioxide	1.5–1.7	0.972, 0.991	Gold/silicon dioxide/Gold	Biosensor for detecting coronaviruses
[83]	SiO_2	0.5–2.5	—	SiO_2/Graphene	Breast cancer detection
[88]	SiO_2	2–6	0.99	graphene/Au/SiO_2/Au	Refractive index sensor
[50]	Glass	0–0.37	0.998	Glass/InSb/MgF2/InSb	Colon Cancer detection
[88]	Photonic crystal plate	1–3	0.97, 0.98, 0.99	bulk Dirac semimetal/ photonic crystal/Au	Narrowband perfect absorber
[89]	Dielectric layer	1–3	0.99, 0.99	Au/dielectric layer/Au	Sensor
[90]	PET	0–3	0.99, 0.80, 0.95	PET/FSS/UV glue/ Graphene	Multifunctional tunable terahertz
[91]	Teflon	0.7–5	> 0.96	Ion gel/Graphene/Teflon/ Gold	Polarisation-sensitive
[92]	Topas spacer	0.5–4.5	0.99, 0.98, 0.99	graphene/Topas/Au	Ultra-broadband absorber
[93]	Dielectric Teflon	1–2.2	0.99	Au/dielectric Teflon/Au	Sensor
This work	PET	0.5–2	0.85, 0.94, 0.96, 0.996, 0.96, 0.95, 0.96, 0.985	Al/PET/Al	Blood cancer, microwave imaging and biosensor

sensing metrics across various metamaterial-based biosensors reported between 2014 and 2023. In this context, the proposed design achieves:

1. Q-factor: 268.34—over 20× higher than typical values reported for THz biosensors, enabling exceptional frequency resolution.
2. Euclidean Sensitivity: 355.859564 THz RIU^{-1}—orders of magnitude greater than prior works, indicating superior separation between healthy and cancerous spectral profiles.
3. FOM (RIU^{-1}): 56722.80—substantially higher than the best-performing literature benchmarks, reflecting unparalleled refractive index sensitivity.

These metrics underscore the synergistic impact of the tri-negative metamaterial design, full-spectrum analysis and AI-assisted classification pipeline. No previously reported biosensor achieves this combination of ultra-high spectral resolution, whole-spectrum sensitivity and real-time AI-driven interpretation for blood cancer detection.

10.5 | Summary of Benchmarking Insights

The benchmarking analysis confirms that the proposed biosensor not only meets but significantly exceeds the state-of-the-art in multiple critical dimensions:

1. *Detection Specificity*: Leukaemia-focused dielectric targeting outperforms generic cancer biosensors.
2. *Diagnostic Stage*: Designed for early-stage intervention, unlike many late-stage-oriented systems.
3. *Data Processing*: Full-spectrum analytical decision-making replaces partial-spectrum, peak-based detection.
4. *Workflow*: Intelligence-first development accelerates optimisation and enhances diagnostic speed.
5. *Sensitivity Metrics*: Record-breaking Q-factor, Euclidean sensitivity and FOM compared to published works.

These results provide strong evidence that the proposed biosensor is well-positioned to become a next-generation diagnostic platform for early-stage leukaemia, offering both superior technical performance and practical advantages for clinical deployment.

11 | Future Perspective

The proposed THz metamaterial biosensor, combined with AI-driven full-spectrum analysis, demonstrates unprecedented sensitivity and specificity for early-stage leukaemia detection. Although simulation-based and preliminary experimental validations confirm its diagnostic potential, several strategic advancements can further enhance its clinical impact and broaden its scope of application.

11.1 | Transition From Simulation to Fabrication

The current design leverages an intelligence-first development model (Table 9), in which AI-assisted spectral interpretation is integrated prior to physical fabrication. The next step involves transitioning to prototype fabrication using advanced lithographic or 3D nano-printing techniques capable of achieving micron-scale precision. This will enable real-world evaluation of the biosensor under controlled laboratory conditions and, subsequently, in clinical pilot studies.

11.2 | Numerical Validation and Mesh Convergence Studies

Although the present work demonstrates consistent electromagnetic behaviour through full-wave simulations and field distribution analysis, further numerical investigations can strengthen the validation of the proposed biosensor. Future work will include narrow-band simulations centred around individual resonance frequencies to further verify the physical origin and stability of the observed absorption peaks. Such analysis will enable the isolation of individual resonance modes and provide additional confirmation that the spectral responses arise from intrinsic electromagnetic mechanisms rather than numerical artefacts.

In addition, systematic mesh convergence studies will be performed using progressively refined mesh configurations and adaptive local refinement techniques. Attention will be given to regions exhibiting strong field localisation, including resonator edges, narrow gaps and discontinuities where electromagnetic behaviour is highly sensitive to geometrical resolution. The influence of mesh density on resonance frequency stability, absorption magnitude, and field confinement characteristics will also be investigated. These analyses will provide additional confidence in the numerical robustness and reproducibility of the proposed biosensor design.

11.3 | Integration Into Portable Diagnostic Platforms

For practical deployment in healthcare settings, the biosensor can be embedded into compact, handheld diagnostic platforms that combine a low-power THz source, integrated metamaterial sensing chip and embedded AI processor. Such platforms could be used in point-of-care environments, including outpatient clinics and remote screening centres, to deliver immediate diagnostic results without the need for centralised laboratory infrastructure.

11.4 | Multiplexed Biomarker Detection

Although the present study focuses on leukaemia-specific dielectric changes, the multiband nature of the metamaterial absorber enables simultaneous detection of multiple biomarkers. By functionalising the sensor surface with selective bio-recognition layers (e.g., antibodies, aptamers), it is possible to expand detection capabilities to other haematological disorders and cancers. This multiplexed sensing approach could facilitate comprehensive blood diagnostics from a single sample, improving efficiency and reducing patient discomfort.

11.5 | Clinical Validation and Regulatory Pathway

Following laboratory validation, clinical trials will be essential to assess diagnostic accuracy, reproducibility and robustness under real-world variability, including differences in patient demographics, blood composition and environmental conditions. Successful trials would pave the way for regulatory approval under relevant medical device frameworks, enabling formal adoption in clinical practice.

11.6 | Long-Term Research Directions

Long-term research should focus on:

1. *Adaptive AI Models*: Developing self-learning algorithms capable of updating classification thresholds as new patient data is acquired, ensuring sustained accuracy over time.
2. *THz Hardware Optimisation*: Exploring low-cost, tunable THz sources and detectors to reduce system size, cost and power consumption.
3. *Cross-Disease Applications*: Applying the same sensing and AI framework to diagnose other cancers (e.g., breast, cervical, skin) and infectious diseases where dielectric contrasts are diagnostically relevant.

11.7 | Vision for Next-Generation Blood Diagnostics

Ultimately, the integration of high-Q metamaterial sensing, full-spectrum dielectric analysis, and real-time AI classification could redefine the standard of care for blood cancer detection. By enabling rapid, noninvasive, and highly accurate diagnostics at the earliest stages of disease progression, such systems have the potential to dramatically improve survival rates, reduce treatment costs and enhance global access to quality healthcare.

12 | Conclusions

This work has presented the design, simulation and evaluation of an AI-augmented micron-scale THz metamaterial biosensor for the early-stage diagnosis of leukaemia. By integrating a tri-negative (ε, μ, n) perfect absorber with a multiband spectral response and coupling it to a full-spectrum, AI-driven diagnostic framework, the proposed system achieves an unprecedented combination of sensitivity, specificity, and real-time interpretive capability. The engineered metamaterial absorber demonstrates simultaneous negative permittivity, permeability, and refractive index in targeted THz bands, producing high-Q, narrowband resonances that amplify interactions between incident THz waves and biological analytes. This structural and electromagnetic innovation enables the biosensor to resolve minute refractive index differences (~0.014 RIU) between normal and leukaemia-affected blood, as demonstrated in Figures 33–37, with measurable resonance shifts, increased absorption depths, and altered E-field/H-field distributions.

Quantitative benchmarking (Table 6) confirms record-setting values for Q-factor (268.34), Euclidean sensitivity (355.859564 THz RIU^{-1}), and FOM (56722.80 RIU^{-1}), surpassing all reported THz biosensors for cancer detection between 2014 and 2023. The AI integration, detailed in Sections 7 and 8, leverages both S-parameter vector analysis and full-spectrum similarity metrics (MSE, Euclidean distance, correlation) to classify unknown samples with over 95% simulated accuracy. This automated approach eliminates manual thresholding, increases adaptability and enables real-time diagnosis. Comparative analysis with existing biosensors (Tables 8 and 9) confirms the unique strengths of this work: leukaemia-specific dielectric targeting, early-stage detection capability, whole-spectrum decision-making and intelligence-first development methodology.

Collectively, these contributions establish a new paradigm in metamaterial biosensing, moving from static, fabrication-first devices to dynamic, AI-enhanced platforms that are adaptable, scalable and clinically relevant. The results suggest a clear pathway toward noninvasive, label-free, point-of-care diagnostics capable of detecting blood cancers at their earliest stages when treatment outcomes are most favourable. Future work will focus on transitioning from simulation to fabrication, integrating the sensor into portable diagnostic units, and conducting clinical trials to validate performance in diverse patient populations. Given its high sensitivity, specificity and adaptability, the proposed biosensor holds significant promise for transforming not only leukaemia screening but also broader haematological and oncological diagnostics.

Author Contributions

Musa N. Hamza: conceptualization, data curation, formal analysis, investigation, methodology, resources, software, validation, visualization, writing – original draft. **Mohammad Alibakhshikenari:** conceptualization, data curation, formal analysis, funding acquisition, investigation, methodology, project administration, resources, software, validation, visualization, writing – original draft. **Bal Virdee:** conceptualization, data curation, formal analysis, investigation, methodology, resources, validation, writing – review and editing. **Sunil Lavadiya:** conceptualization, formal analysis, methodology, validation, visualization, writing – review and editing. **Iftikhar ud Din:** conceptualization, data curation, investigation, resources, validation, writing – review and editing. **Bruno Sanches:** formal analysis, methodology, resources, validation, visualization, writing – review and editing. **Slawomir Koziel:** formal analysis, investigation, supervision, validation, visualization, writing – review and editing. **Syeda Iffat Naqvi:** conceptualization, data curation, methodology, resources, validation, writing – review and editing. **Abinash Panda:** formal analysis, investigation, methodology, validation, writing – review and editing. **Ali Farmani:** data curation, formal analysis, resources, software, validation, writing – review and editing. **Zinelabiddine Mezache:** conceptualization, methodology, resources, validation, writing – review and editing. **Hassan Zakeri:** conceptualization, formal analysis, methodology, software, validation, writing – review and editing. **Mohammad Naser-Moghadasi:** conceptualization, data curation, methodology, resources, validation, writing – review and editing. **Takfarinas Saber:** conceptualization, formal analysis, investigation, supervision, validation, writing – review and editing.

Funding

Dr. Mohammad Alibakhshikenari is co-funded by the European Union. Views and opinions expressed are however, those of the author(s) only and do not necessarily reflect those of the European Union or the European Research Executive Agency. Neither the European Union nor the granting authority can be held responsible for them. Besides that, Dr. Mohammad Alibakhshikenari has emanated from research jointly funded by Taighde Éireann – Research Ireland under Grant No. 13/RC/2094_2, the European Union's Marie Sklodowska-Curie Actions under Grant No. 101126578 and was supported in part by University of Galway. In addition, this research is supported by the Icelandic Research Fund Grant 239858, and National Science Centre of Poland Grant 2020/37/B/ST7/01448.

Conflicts of Interest

The authors declare no conflicts of interest.

Data Availability Statement

The data that support the findings of this study are available from the corresponding author upon reasonable request.

References

1. S. Deo, J. Sharma, and S. Kumar, "GLOBOCAN 2020 Report on Global Cancer Burden: Challenges and Opportunities for Surgical Oncologists," *Annals of Surgical Oncology* 29, no. 11 (2022): 6497–6500, https://doi.org/10.1245/s10434-022-12151-6.

2. D. A. Milner and J. K. Lennerz, "Technology and Future of Multi-Cancer Early Detection," *Life* 14, no. 7 (2024): 833, https://doi.org/10.3390/life14070833.

3. A. Pulumati, A. Pulumati, B. S. Dwarakanath, A. Verma, and R. V. Papineni, "Technological Advancements in Cancer Diagnostics: Improvements and Limitations," *Cancer Reports* 6, no. 2 (2023): e1764, https://doi.org/10.1002/cnr2.1764.

4. X. Liu, H. Jiang, and X. Wang, "Advances in Cancer Research: Current and Future Diagnostic and Therapeutic Strategies," *Biosensors* 14, no. 2 (2024): 100, https://doi.org/10.3390/bios14020100.

5. J. Ferlay, M. Colombet, I. Soerjomataram, et al., "Cancer Statistics for the Year 2020: An Overview," *International Journal of Cancer* 149, no. 4 (2021): 778–789, https://doi.org/10.1002/ijc.33588.

6. M. Badwelan, H. Muaddi, A. Ahmed, K. T. Lee, and S. D. Tran, "Oral Squamous Cell Carcinoma and Concomitant Primary Tumors, what do we Know? A Review of the Literature," *Current Oncology* 30, no. 4 (2023): 3721–3734, https://doi.org/10.3390/curroncol30040283.

7. A. Barsouk, J. S. Aluru, P. Rawla, K. Saginala, and A. Barsouk, "Epidemiology, Risk Factors, and Prevention of Head and Neck Squamous Cell Carcinoma," *Medical Sciences* 11, no. 2 (2023): 42, https://doi.org/10.3390/medsci11020042.

8. E. Merry, K. Thway, R. L. Jones, and P. H. Huang, "Predictive and Prognostic Transcriptomic Biomarkers in Soft Tissue Sarcomas," *npj Precision Oncology* 5, no. 1 (2021): 17, https://doi.org/10.1038/s41698-021-00157-4.

9. H. K. Birdi, A. Jirovec, S. Cortés-Kaplan, et al., "Immunotherapy for Sarcomas: New Frontiers and Unveiled Opportunities," *Journal for immunotherapy of cancer* 9, no. 2 (2021): e001580, https://doi.org/10.1136/jitc-2020-001580.

10. C. K. Tebbi, "Etiology of Acute Leukemia: A Review," *Cancers* 13, no. 9 (2021): 2256, https://doi.org/10.3390/cancers13092256.

11. S. A. Atallah-Yunes and M. J. Robertson, "Cytokine Based Immunotherapy for Cancer and Lymphoma: Biology, Challenges and Future Perspectives," *Frontiers in Immunology* 13 (2022): 872010, https://doi.org/10.3389/fimmu.2022.872010.

12. M. H. Jagosky and S. Z. Usmani, "Extramedullary Disease in Multiple Myeloma," *Current Hematologic Malignancy Reports* 15, no. 2 (2020): 62–71, https://doi.org/10.1007/s11899-020-00568-3.

13. F. Ishida, "Aggressive NK-cell Leukemia," *Frontiers in Pediatrics* 6 (2018): 292, https://doi.org/10.3389/fped.2018.00292.

14. V. Stavropoulou, A. H. Peters, and J. Schwaller, "Aggressive Leukemia Driven by MLL-AF9," *Molecular & Cellular Oncology* 5, no. 3 (2018): e1241854, https://doi.org/10.1080/23723556.2016.1241854.

15. X. Chen, J. Gole, A. Gore, et al., "Non-Invasive Early Detection of Cancer Four Years Before Conventional Diagnosis Using a Blood Test," *Nature Communications* 11, no. 1 (2020): 1–10, https://doi.org/10.1038/s41467-020-17316-z.

16. V. Acharya, V. Ravi, T. D. Pham, and C. Chakraborty, "Peripheral Blood Smear Analysis Using Automated Computer-Aided Diagnosis System to Identify Acute Myeloid Leukemia," *IEEE Transactions on Engineering Management* 70, no. 8 (2021): 2760–2773, https://doi.org/10.1109/tem.2021.3103549.

17. M.-E. Percival, C. Lai, E. Estey, and C. S. Hourigan, "Bone Marrow Evaluation for Diagnosis and Monitoring of Acute Myeloid Leukemia," *Blood Reviews* 31, no. 4 (2017): 185–192, https://doi.org/10.1016/j.blre.2017.01.003.

18. P. R. Gonzales and F. M. Mikhail, "Diagnostic and Prognostic Utility of Fluorescence in Situ Hybridization (FISH) Analysis in Acute Myeloid Leukemia," *Current Hematologic Malignancy Reports* 12, no. 6 (2017): 568–573, https://doi.org/10.1007/s11899-017-0426-6.

19. I. Della Starza, V. Nunes, F. Lovisa, et al., "Droplet Digital PCR Improves IG-/TR-based MRD Risk Definition in Childhood B-Cell Precursor Acute Lymphoblastic Leukemia," *HemaSphere* 5, no. 3 (2021): e543, https://doi.org/10.1097/hs9.0000000000000543.

20. Q. Cai, H. Lan, D. Yi, et al., "Flow Cytometry in Acute Myeloid Leukemia and Detection of Minimal Residual Disease," *Clinica Chimica Acta* 564 (2025): 119945, https://doi.org/10.1016/j.cca.2024.119945.

21. G. K. Gupta, X. Sun, C. M. Yuan, M. Stetler-Stevenson, R. J. Kreitman, and I. Maric, "Usefulness of Dual Immunohistochemistry Staining in Detection of Hairy Cell Leukemia in Bone Marrow," *American Journal of Clinical Pathology* 153, no. 3 (2020): 322–327, https://doi.org/10.1093/ajcp/aqz171.

22. V. Kumar, D. Kukkar, B. Hashemi, K. H. Kim, and A. Deep, "Advanced Functional Structure-Based Sensing and Imaging Strategies for Cancer Detection: Possibilities, Opportunities, Challenges, and Prospects," *Advanced Functional Materials* 29, no. 16 (2019): 1807859, https://doi.org/10.1002/adfm.201807859.

23. V. S. A. Jayanthi, A. B. Das, and U. Saxena, "Recent Advances in Biosensor Development for the Detection of Cancer Biomarkers," *Biosensors and Bioelectronics* 91 (2017): 15–23, https://doi.org/10.1016/j.bios.2016.12.014.

24. C.-W. Huang, C. Lin, M. K. Nguyen, A. Hussain, X.-T. Bui, and H. H. Ngo, "A Review of Biosensor for Environmental Monitoring: Principle, Application, and Corresponding Achievement of Sustainable Development Goals," *Bioengineered* 14, no. 1 (2023): 58–80, https://doi.org/10.1080/21655979.2022.2095089.

25. M. R. Rakhshani and M. A. Mansouri-Birjandi, "Engineering Hexagonal Array of Nanoholes for High Sensitivity Biosensor and Application for Human Blood Group Detection," *IEEE Transactions on Nanotechnology* 17, no. 3 (2018): 475–481, https://doi.org/10.1109/tnano.2018.2811800.

26. A. Curulli, "Electrochemical Biosensors in Food Safety: Challenges and Perspectives," *Molecules* 26, no. 10 (2021): 2940, https://doi.org/10.3390/molecules26102940.

27. R. Goldoni, A. Scolaro, E. Boccalari, et al., "Malignancies and Biosensors: A Focus on Oral Cancer Detection Through Salivary Biomarkers," *Biosensors* 11, no. 10 (2021): 396, https://doi.org/10.3390/bios11100396.

28. A. Roointan, T. Ahmad Mir, S. Ibrahim Wani, et al., "Early Detection of Lung Cancer Biomarkers Through Biosensor Technology: A Review," *Journal of Pharmaceutical and Biomedical Analysis* 164 (2019): 93–103, https://doi.org/10.1016/j.jpba.2018.10.017.

29. Z. Zhang, Q. Li, X. Du, and M. Liu, "Application of Electrochemical Biosensors in Tumor Cell Detection," *Thoracic Cancer* 11, no. 4 (2020): 840–850, https://doi.org/10.1111/1759-7714.13353.

30. N. Altunkök, Ö. B. Ünlüer, E. B. Özkütük, and A. Ersöz, "Development of Potentıometrıc Bıosensor for Dıagnosıs of Prostate Cancer," *Materials Science and Engineering: B* 263 (2021): 114789, https://doi.org/10.1016/j.mseb.2020.114789.

31. L. Zou, X. Liu, Y. Zhou, et al., "Optical Fiber Amplifier and Thermometer Assisted Point-of-Care Biosensor for Detection of Cancerous Exosomes," *Sensors and Actuators B: Chemical* 351 (2022): 130893, https://doi.org/10.1016/j.snb.2021.130893.

32. M. Y. Azab, M. F. O. Hameed, and S. S. Obayya, "Overview of Optical Biosensors for Early Cancer Detection: Fundamentals, Applications and Future Perspectives," *Biology* 12, no. 2 (2023): 232, https://doi.org/10.3390/biology12020232.

33. A. Bijalwan, B. K. Singh, and V. Rastogi, "Analysis of One-Dimensional Photonic Crystal Based Sensor for Detection of Blood Plasma and Cancer Cells," *Optik* 226 (2021): 165994, https://doi.org/10.1016/j.ijleo.2020.165994.

34. S. A. Khan, N. Z. Khan, Y. Xie, et al., "Optical Sensing by Metamaterials and Metasurfaces: From Physics to Biomolecule Detection," *Advanced Optical Materials* 10, no. 18 (2022): 2200500, https://doi.org/10.1002/adom.202200500.

35. M. Beheshti Asl, J. Karamdel, M. Khoshbaten, and A. Rostami, "Plasmonic Biosensor for Early Gastric Cancer Detection," *Optics Continuum* 1, no. 9 (2022): 2043–2061, https://doi.org/10.1364/optcon.462176.

36. A. Salim and S. Lim, "Recent Advances in the Metamaterial-Inspired Biosensors," *Biosensors and Bioelectronics* 117 (2018): 398–402, https://doi.org/10.1016/j.bios.2018.06.031.

37. S. Shamim, A. S. Mohsin, M. M. Rahman, and M. B. H. Bhuian, "Recent Advances in the Metamaterial and Metasurface-Based Biosensor in the Gigahertz, Terahertz, and Optical Frequency Domains," *Heliyon* 10, no. 13 (2024): e33272, https://doi.org/10.1016/j.heliyon.2024.e33272.

38. A. Hoque, M. T. Islam, A. F. Almutairi, M. E. Chowdhury, and M. Samsuzzaman, "SNG and DNG Meta-Absorber With Fractional Absorption Band for Sensing Application," *Scientific Reports* 10, no. 1 (2020): 13086, https://doi.org/10.1038/s41598-020-69792-4.

39. M. L. Hakim, T. Alam, M. S. Soliman, et al., "Polarization Insensitive Symmetrical Structured Double Negative (DNG) Metamaterial Absorber for Ku-Band Sensing Applications," *Scientific Reports* 12, no. 1 (2022): 479, https://doi.org/10.1038/s41598-021-04236-1.

40. Y. Peng, C. Shi, X. Wu, Y. Zhu, and S. Zhuang, "Terahertz Imaging and Spectroscopy in Cancer Diagnostics: A Technical Review," *BME Frontiers* 2020 (2020): 2547609, https://doi.org/10.34133/2020/2547609.

41. M. Gezimati and G. Singh, "Advances in Terahertz Technology for Cancer Detection Applications," *Optical and Quantum Electronics* 55, no. 2 (2023): 151, https://doi.org/10.1007/s11082-022-04340-0.

42. Z. Zhang, R. Zhao, M. Cong, and J. Qiu, "Developments of Terahertz Metasurface Biosensors: A Literature Review," *Nanotechnology Reviews* 13, no. 1 (2024): 20230182, https://doi.org/10.1515/ntrev-2023-0182.

43. H. Chen, R. N. Kostoff, C. Chen, et al., "AI and Global Science and Technology Assessment," *IEEE Intelligent Systems* 24, no. 4 (2009): 68–88, https://doi.org/10.1109/mis.2009.68.

44. Y. Xu, X. Liu, X. Cao, et al., "Artificial Intelligence: A Powerful Paradigm for Scientific Research," *Innovation* 2, no. 4 (2021): 100179, https://doi.org/10.1016/j.xinn.2021.100179.

45. P. Apell and H. Eriksson, "Artificial Intelligence (AI) Healthcare Technology Innovations: The Current State and Challenges From a Life Science Industry Perspective," *Technology Analysis & Strategic Management* 35, no. 2 (2023): 179–193, https://doi.org/10.1080/09537325.2021.1971188.

46. N. Kalra, P. Verma, and S. Verma, "Advancements in AI Based Healthcare Techniques With Focus On Diagnostic Techniques," *Computers in Biology and Medicine* 179 (2024): 108917, https://doi.org/10.1016/j.compbiomed.2024.108917.

47. A. Holzinger, K. Keiblinger, P. Holub, K. Zatloukal, and H. Müller, "AI for Life: Trends in Artificial Intelligence for Biotechnology," *New Biotechnology* 74 (2023): 16–24, https://doi.org/10.1016/j.nbt.2023.02.001.

48. M. S. Alshuhri, S. G. Al-Musawi, A. A. Al-Alwany, et al., "Artificial Intelligence in Cancer Diagnosis: Opportunities and Challenges," *Pathology, Research & Practice* 253 (2024): 154996, https://doi.org/10.1016/j.prp.2023.154996.

49. B. Hunter, S. Hindocha, and R. W. Lee, "The Role of Artificial Intelligence in Early Cancer Diagnosis," *Cancers* 14, no. 6 (2022): 1524, https://doi.org/10.3390/cancers14061524.

50. Z. Vafapour, W. Troy, and A. Rashidi, "Colon Cancer Detection by Designing and Analytical Evaluation of a Water-Based THz Metamaterial Perfect Absorber," *IEEE Sensors Journal* 21, no. 17 (2021): 19307–19313, https://doi.org/10.1109/jsen.2021.3087953.

51. S. Nourinovin, M. M. Rahman, M. Naftaly, M. P. Philpott, Q. H. Abbasi, and A. Alomainy, "Highly Sensitive Terahertz Metasurface Based on Electromagnetically Induced Transparency-Like Resonance in Detection of Skin Cancer Cells," *IEEE Transactions on Biomedical Engineering* (2024).

52. H. Bahador, "Five-Segment THz Refractive Index Metamaterial Biosensor With Perfect Absorption for Carcinoembryonic Antigen Measurement," *IEEE Sensors Journal* (2024).

53. S. Lokesh, B. Sathyasri, G. Christina, and T. D. Kumar, "Metamaterial Cavity Based EBG Loaded THz Breast and Skin Cancer Biosensor With High Q-Factor," *Microsystem Technologies* 31, no. 9 (2025): 1–11, https://doi.org/10.1007/s00542-025-05855-8.

54. S. K. Patel and O. Alsalman, "Design and Development of Graphene-Based Double Split Ring Resonator Metasurface Biosensor Using MgF2-Gold Materials for Blood Cancer Detection," *Optical and Quantum Electronics* 56, no. 7 (2024): 1120, https://doi.org/10.1007/s11082-024-07068-1.

55. M. N. Hamza and M. T. Islam, "Design of MTM-Based Multi-Band Micro-Biosensor in Terahertz Region as Perfect Absorber for Early-Stage Leukemia Diagnosis With Sensitivity 18626373 THz/RIU," *IEEE Sensors Journal* (2024).

56. O. Alsalman, "Graphene-Based Surface Plasmon Resonance Biosensor Design Using Square-Shaped Metamaterial Resonators for Blood Cancer Detection," *Plasmonics* 20, no. 9 (2025): 1–11, https://doi.org/10.1007/s11468-024-02652-3.

57. M. N. Hamza, "Development of a High-Sensitivity Triple-Band Nano-Biosensor Utilizing Petahertz Metamaterials for Optimal Absorption in Early-Stage Leukemia Detection," *IEEE Sensors Journal* (2025).

58. P. P. Kumar, S. R. Eedala, A. Yammanuru, A. N. Grace, and A. C. J. Malathi, "Non-Invasive Leukemia Detection via CSRR Sensor," *Journal of Hazardous Materials Advances* 18 (2025): 100654, https://doi.org/10.1016/j.hazadv.2025.100654.

59. N. Houssami, G. Kirkpatrick-Jones, N. Noguchi, and C. I. Lee, "Artificial Intelligence (AI) for the Early Detection of Breast Cancer: A Scoping Review to Assess Ai's Potential in Breast Screening Practice," *Expert Review of Medical Devices* 16, no. 5 (2019): 351–362, https://doi.org/10.1080/17434440.2019.1610387.

60. C. Mondal, M. K. Hasan, M. Ahmad, et al., "Ensemble of Convolutional Neural Networks to Diagnose Acute Lymphoblastic Leukemia From Microscopic Images," *Informatics in Medicine Unlocked* 27 (2021): 100794, https://doi.org/10.1016/j.imu.2021.100794.

61. Z. Zhu, Y. Sun, and B. Honarvar Shakibaei Asli, "Early Breast Cancer Detection Using Artificial Intelligence Techniques Based on Advanced Image Processing Tools," *Electronics* 13, no. 17 (2024): 3575, https://doi.org/10.3390/electronics13173575.

62. M. S. Hamdi, A. Bouali, and F. AbdelMalek, "A Machine Learning Approach for Enhanced Early Detection of Cancerous Cells Using Optimized Metamaterial Graphene Biosensors," *Discover Sensors* 1, no. 1 (2025): 6, https://doi.org/10.1007/s44397-025-00006-0.

63. J. P. Appadurai, K. Kaliaperumal, J. Wekalao, and A. Rajakannu, "Artificial Intelligence-Enhanced Terahertz Metasurface Biosensor for Breast Cancer Biomarker Detection," *Plasmonics* 21 (2025): 1–14, https://doi.org/10.1007/s11468-025-03051-y.

64. S. Banerjee, M. S. Khan, U. Nath, S. K. Mishra, and B. Appasani, "Skin Cancer Detection Using Terahertz Metamaterial Absorber and Machine Learning," *IEEE Transactions on Plasma Science* (2025).

65. J. Wekalao, H. A. Elsayed, A. M. El-Sherbeeny, M. R. Abukhadra, and A. Mehaney, "Design and Optimization of a Graphene-Enhanced Terahertz Metasurfaces Surface Plasmon Resonance Biosensor With Multi-Material Architecture for Cancer Detection Integrating 1D-CNN Machine Learning for Performance Prediction and Analysis," *Plasmonics* 21 (2025): 1–23, https://doi.org/10.1007/s11468-025-02912-w.

66. F. Jafrasteh, A. Farmani, and J. Mohamadi, "Meticulous Research for Design of Plasmonics Sensors for Cancer Detection and Food Contaminants Analysis via Machine Learning and Artificial Intelligence," *Scientific Reports* 13, no. 1 (2023): 15349, https://doi.org/10.1038/s41598-023-42699-6.

67. J. Wekalao, A. H. M. Almawgani, R. Ghodhbani, et al., "Graphene-Based Metasurface Terahertz Biosensing Platform for Accurate Alpha-Fetoprotein Detection in Liver Cancer Diagnosis Enhanced With Machine Learning Optimization," *Plasmonics* 20, no. 8 (2025): 1–14, https://doi.org/10.1007/s11468-025-02968-8.

68. K. Kishore and G. Varshney, "Thermal Dispersive Variation in Quality Factor of Resonances for Broad and Multiband THz Absorber," *IEEE Transactions on Plasma Science* 54, no. 4 (April 2026): 1745–1749, https://doi.org/10.1109/TPS.2026.3669965.

69. P. K. Singh and G. Varshney, "Multicontrolled Multiresonance Generation in THz Metamaterial Absorber," *IEEE Transactions on Plasma Science* 54, no. 4 (April 2026): 1785–1791, https://doi.org/10.1109/TPS.2026.3669967.

70. M. F. Ali, A. Singh, P. Giri, and G. Varshney, "Graphene Supported Ultrathin VO_2 Resonators for Multifunctional THz Absorption," *IEEE Transactions on Plasma Science* 52, no. 2 (February 2024): 545–552, https://doi.org/10.1109/TPS.2023.3342115.

71. S. K. Patel, J. Surve, and J. Parmar, "Detection of Cancer With Graphene Metasurface-Based Highly Efficient Sensors," *Diamond and Related Materials* 129 (2022): 109367, https://doi.org/10.1016/j.diamond.2022.109367.

72. T. Chen, D. Zhang, F. Huang, Z. Li, and F. Hu, "Design of a Terahertz Metamaterial Sensor Based on Split Ring Resonator Nested Square Ring Resonator," *Materials Research Express* 7, no. 9 (2020): 095802, https://doi.org/10.1088/2053-1591/abb496.

73. S. Park, J. T. Hong, S. J. Choi, et al., "Detection of Microorganisms Using Terahertz Metamaterials," *Scientific Reports* 4, no. 1 (2014): 4988, https://doi.org/10.1038/srep04988.

74. S. Park, S. Cha, G. Shin, and Y. Ahn, "Sensing Viruses Using Terahertz nano-gap Metamaterials," *Biomedical Optics Express* 8, no. 8 (2017): 3551–3558, https://doi.org/10.1364/boe.8.003551.

75. S. Asgari, N. Granpayeh, and T. Fabritius, "Controllable Terahertz Cross-Shaped Three-Dimensional Graphene Intrinsically Chiral Metastructure and its Biosensing Application," *Optics Communications* 474 (2020): 126080, https://doi.org/10.1016/j.optcom.2020.126080.

76. Z. Mezache, Z. Hafdi, and J. Tao, "Design of a Novel Graphene Buzzle Metamaterial Refractometer for Sensing of Cancerous Cells in the Terahertz Regime," *Optik* 287 (2023): 171170, https://doi.org/10.1016/j.ijleo.2023.171170.

77. J. Yang and Y.-S. Lin, "Design of Tunable Terahertz Metamaterial Sensor With Single-and Dual-Resonance Characteristic," *Nanomaterials* 11, no. 9 (2021): 2212, https://doi.org/10.3390/nano11092212.

78. D. Li, F. Hu, H. Zhang, et al., "Identification of Early-Stage Cervical Cancer Tissue Using Metamaterial Terahertz Biosensor With Two Resonant Absorption Frequencies," *IEEE Journal of Selected Topics in Quantum Electronics* 27, no. 4 (2021): 1–7, https://doi.org/10.1109/jstqe.2021.3058163.

79. E. Hoseini, A. Mir, and A. Farmani, "Modeling and Proposal of a Black Phosphorus-Based Nanostructure for Detection of Avian Influenza Virus in Infrared Region," *Optical and Quantum Electronics* 54, no. 10 (2022): 609, https://doi.org/10.1007/s11082-022-04035-6.

80. R. Bhati and A. K. Malik, "Ultra-Efficient Terahertz Metamaterial Sensor," *Results in Optics* 8 (2022): 100236, https://doi.org/10.1016/j.rio.2022.100236.

81. H. Hu, B. Qi, Y. Zhao, X. Zhang, Y. Wang, and X. Huang, "A Graphene-Based THz Metasurface Sensor With Air-Spaced Structure," *Frontiers in Physics* 10 (2022): 990126, https://doi.org/10.3389/fphy.2022.990126.

82. Y. Shen, X. Li, J. Wang, et al., "Low-Concentration Biological Sample Detection Using an Asymmetric Split Resonator Terahertz Metamaterial," *Photonics* 10, no. 2 (2023): 111, https://doi.org/10.3390/photonics10020111.

83. C. Tan, S. Wang, S. Li, et al., "Cancer Diagnosis Using Terahertz-Graphene-Metasurface-Based Biosensor With Dual-Resonance Response," *Nanomaterials* 12, no. 21 (2022): 3889, https://doi.org/10.3390/nano12213889.

84. M. N. Hamza and M. T. Islam, "Designing an Extremely Tiny Dual-Band Biosensor Based on MTMs in the Terahertz Region as a Perfect Absorber for Non-Melanoma Skin Cancer Diagnostics," *IEEE Access* 11 (2023): 136770–136781, https://doi.org/10.1109/access.2023.3339562.

85. Z. Chen, P. Cai, Q. Wen, et al., "Graphene Multi-Frequency Broadband and Ultra-Broadband Terahertz Absorber Based on Surface Plasmon Resonance," *Electronics* 12, no. 12 (2023): 2655, https://doi.org/10.3390/electronics12122655.

86. Z. El-Wasif, T. Ismail, and O. Hamdy, "Design and Optimization of Highly Sensitive Multi-Band Terahertz Metamaterial Biosensor for Coronaviruses Detection," *Optical and Quantum Electronics* 55, no. 7 (2023): 604, https://doi.org/10.1007/s11082-023-04906-6.

87. M. Y. Azab, M. F. O. Hameed, A. M. Nasr, and S. Obayya, "Highly Sensitive Metamaterial Biosensor for Cancer Early Detection," *IEEE Sensors Journal* 21, no. 6 (2021): 7748–7755, https://doi.org/10.1109/jsen.2021.3051075.

88. M.-R. Nickpay, M. Danaie, and A. Shahzadi, "Highly Sensitive THz Refractive Index Sensor Based on Folded Split-Ring Metamaterial Graphene Resonators," *Plasmonics* 17 (2021): 1–12, https://doi.org/10.1007/s11468-021-01512-8.

89. B.-X. Wang, Y. He, P. Lou, and W. Xing, "Design of a Dual-Band Terahertz Metamaterial Absorber Using Two Identical Square Patches for Sensing Application," *Nanoscale Advances* 2, no. 2 (2020): 763–769, https://doi.org/10.1039/c9na00770a.

90. S. Zhuang, X. Li, T. Yang, et al., "Graphene-Based Absorption–Transmission Multi-Functional Tunable THz Metamaterials," *Micromachines* 13, no. 8 (2022): 1239, https://doi.org/10.3390/mi13081239.

91. S. Asgari and T. Fabritius, "Numerical Simulation and Equivalent Circuit Model of Multi-Band Terahertz Absorber Composed of Double-Sided Graphene Comb Resonator Array," *IEEE Access* (2023).

92. L. Liu, W. Liu, and Z. Song, "Ultra-Broadband Terahertz Absorber Based on a Multilayer Graphene Metamaterial," *Journal of Applied Physics* 128, no. 9 (2020): 093104, https://doi.org/10.1063/5.0019902.

93. A. S. Saadeldin, M. F. O. Hameed, E. M. Elkaramany, and S. S. Obayya, "Highly Sensitive Terahertz Metamaterial Sensor," *IEEE Sensors Journal* 19, no. 18 (2019): 7993–7999, https://doi.org/10.1109/jsen.2019.2918214.